A Dissertation Submitted for the Degree of Bachelor

Wind field and performance analysis of air-cooled fuel cell system

By

Hou Zhihao

Hefei University of Technology

Hefei, Anhui, P.R.China

May, 2022

ABSTRACT

Since the 21st century, the demand for energy security applications has expanded and the environmental pollution caused by industrialization has become increasingly serious. Countries all over the world are actively looking for alternative clean new energy sources, among which fuel cell [1] is known as the ultimate energy solution, especially hydrogen fuel cell is the best solution. The unique structural design of the air-cooled fuel cell, which combines the cooling function with the cathode flow channel, makes the oxidant and coolant required by the stack reaction supplied by the cathode fan, but its wind field and performance need to be studied. In this paper, the 500W PEMFC measurement and control platform is used to carry out performance experiments, and the data of single voltage, stack temperature and electric power of fuel cells are recorded with time. The data are processed by Matlab, and the reasons of its performance are analyzed. The results show that

Solidworks is used for modeling, Fluent software is used for grid division, and the wind speed field is solved by changing the wind speed of cathode fan. The distribution of micro-channel wind field and the cause of streamline diagram are mainly analyzed. The results show that the wind field on both sides of the microchannel is relatively vigorous, and the wind speed on the side attached to the wall develops well because the wall surface is fixed without slippage, while the wind field on the middle side of the microchannel develops slowly due to the influence of two large vortices, which is quite different from the actual work requirements.

Finally, the results and conclusions of the project are summarized, and the improvement measures and development direction of the system are put forward.

KEYWORDS: hydrogen energy; Air-cooled fuel cells; Performance analysis;Wind field simulation

1. Introduction

1.1 Research background and significance

At this stage of social development, all industries are experiencing unprecedented rapid growth. The development of new-generation technologies and industrial upgrades following the Third Industrial Revolution are a major driving force behind my country's high-quality economic development. To achieve carbon neutrality and carbon peak targets as quickly as possible, innovations in hydrogen energy development and utilization technologies, represented by fuel cells, have made an invaluable contribution, providing new and feasible approaches to new energy utilization worldwide. Therefore, my country should vigorously support and develop the hydrogen energy industry to achieve widespread clean energy utilization and realize national development transformation as soon as possible.

Globally, major developed countries like Europe and the United States are placing significant emphasis on the development and research of clean energy, including hydrogen, in their own development. As a complementary alternative to fossil fuels, hydrogen energy is a crucial national policy for promoting healthy ecological and economic development and ensuring vigilance in national energy development. Consequently, fuel cell sales have been booming internationally, and key technologies across the hydrogen energy industry chain are undergoing rapid iteration and updates. As hydrogen energy infrastructure becomes more widespread and comprehensive, the use of hydrogen energy will soon become an integral part of our lives.

On the other hand, my country is the country with the largest hydrogen production in the world, with an annual output of 33 million tons, of which about 12 million tons meet and can be used for industrial use standards. In addition, my country ranks first in the world in the number of secondary energy equipment, so in the field of clean energy, China's hydrogen energy supply has irreplaceable advantages. In recent years, with the support of national policies, the entire domestic hydrogen energy industry has ushered in a warm spring period. It has gradually mastered cutting-edge technologies and production processes such as hydrogen preparation, transportation and storage, increasing hydrogen volume, and integration and optimization of hydrogen fuel cell systems. Pilot projects for the application and promotion of fuel cells have been carried out in some cities, which are mainly distributed in the southeast coast and the capital economic circle.

Although the overall development trend is positive and the development momentum is strong, my country's international market competitiveness is weaker than the international advanced level in the direction of industrial innovation and research and development. Compared with foreign countries that have developed for decades and have a complete industrial chain,

supporting policies and equipment base, as well as actual popularization, my country's hydrogen energy industry foundation is slightly weak, with inadequate technical equipment, insufficient increase in innovative technology, and the automobile, drone and other targeted industries that can be used by fuel cells are still in a period of stagnation, resulting in a bottleneck in the development of the hydrogen energy industry. As a new energy technology for the 21st century, the development of the hydrogen energy industry requires the overall coordination of the Party and the State, and it also needs to start from the individual level to optimize users' confidence in the use of hydrogen energy, promote the objective and fair support of the entire society for the hydrogen energy industry, and promote the social economy to develop in an environmentally friendly way.

Just as the recent Russian natural gas outage has impacted European industry and life, with industrial production halted and natural gas unable to be used for heating, 21st-century Europeans are forced to resort to the age-old practice of burning wood for heating, unable to enjoy regular hot showers. This severely impacts daily life, and means of transportation, such as cars, are rendered inoperable by the lack of oil and other supplies. As we know, for us in the industrial age, energy is inextricably linked to our work and lives, guaranteeing our enjoyment of modern life. Therefore, how to develop and utilize it has always been a key concern. However, with the ever-increasing demand for energy, over-exploitation of primary energy sources such as oil and coal has caused irreversible damage to the original ecological environment in the mining areas and caused long-term environmental pollution. According to my country's "dual carbon" policy, announced in September 2020, which aims to achieve carbon peak by 2030 and carbon neutrality by 2060, the transformation of traditional energy sources and the transformation of the energy structure are imminent. Consequently, the development and utilization of clean energy are gaining increasing attention. However, compared to hydrogen, clean energy sources such as solar and wind power often exhibit certain volatility and discontinuity, thus significantly limiting their application. Unlike other energy sources, hydrogen can be produced in a variety of ways. It can be produced from traditional fossil fuels or purified from industrial waste gas through methods such as pressure swing adsorption. Furthermore, hydrogen can be obtained from renewable energy sources, such as electrolysis of water using the large amount of waste hydropower generated during hydroelectric power generation, or directly from solar energy through photochemical and photothermolysis technologies. Therefore, hydrogen energy can effectively promote energy structural transformation and green development. Hydrogen energy can be quickly and easily converted into electricity and heat, boasting a high conversion efficiency compared to the less than 35% energy conversion rate of traditional internal combustion engines. More importantly, the conversion process does not produce greenhouse

gases such as CO2, making it environmentally friendly and pollution-free. After extensive practical application and development, hydrogen energy is now widely used in various applications, including transportation, portable power supplies, and stationary power stations. Its production, transportation, storage, and use are increasing in scale, making it of great strategic significance for optimizing energy structure and sustainable development.

In the current technological development, the research and commercial application of fuel cells in the field of hydrogen energy utilization is the most mature, attracting widespread attention from all walks of life. The popularity and widespread acclaim of fuel cells stems not only from their clean, pollution-free reaction process and high conversion efficiency, but also from their superior sustainable power generation. Compared to secondary batteries like lithium batteries, fuel cells are free from the constraint of periodic capacity replenishment. As long as the fuel gas is continuously flowing into the reactor stack, the fuel cell can continuously react, unrestricted by capacity. This significant advantage in power generation further expands the scope of their applications. Furthermore, among various energy conversion devices, fuel cell cells have a high active area per unit area, enabling efficient power output during the conversion of chemical energy into electrical energy through chemical reactions. This characteristic also makes fuel cells stand out among other energy conversion devices. Furthermore, large fuel cell stacks generate a certain amount of heat during the reaction process. Effectively utilizing this heat can reduce unnecessary losses during the energy conversion process and achieve energy conservation. In recent years, with the development of technology, hydrogen fuel cell vehicles represented by Nikola have developed rapidly, announcing that the development and utilization of hydrogen fuel cells has entered a new era[2].

1.2 Fuel Cell Overview

1.2.1 Fuel cell classification

Fuel cells essentially rely on chemical reactions to generate electricity. The principle is to use the mixed reaction of fuel and oxygen to convert part of the chemical energy in the fuel into electrical energy through redox reaction. According to the different types of electrolytes, current fuel cells are mainly divided into the following six types: proton exchange membrane fuel cells (PEMFC), methanol fuel cells (DMFC), phosphate fuel cells (PAFC), alkaline fuel cells (AFC), molten salt fuel cells (MCFC) and solid oxide fuel cells (SOFC) [3].

(1) As the name suggests, proton exchange membrane fuel cells (PEMFCs) use a proton exchange membrane as their electrolyte. A single cell consists of three components: an anode, a cathode, and the PEM. Most commonly, hydrogen and oxygen react, making them the most widely used fuel cells. Their characteristic is that of the protons and electrons generated by the

anode reaction, only the protons can pass through the PEM to the cathode, achieving redox reactions. The electrons, on the other hand, flow through the device's wires to form an electric current, thereby generating electricity.

(2) Phosphoric acid fuel cells are medium-temperature fuel cells with concentrated phosphoric acid as the electrolyte. The positive and negative electrodes of the cell are identical to precious metal gas diffusion electrodes. Operating at 150-220°C, they offer a high cost-effectiveness ratio. Their stable electrolyte eliminates concerns about diffusion hazards after decomposition. Furthermore, phosphoric acid can be stored in concentrated form, effectively saving storage space. Most importantly, they are not degraded by harmful gases. Operating pressure is reasonable, making them relatively popular in the market.

(3) Alkaline fuel cells are one of the earliest fuel cells to enter the practical stage and are currently one of the most technologically mature fuel cells. Their electrolyte is a strong alkaline solution such as KOH or NaOH, and the electrons generated by the cathode are transferred through OH- ions. Due to their superior performance, they were first used in the automotive field. For example, the Bacon medium-temperature, medium-pressure hydrogen-oxygen fuel cell that powered forklifts in 1959 is an alkaline fuel cell.

(4) Solid oxide fuel cells are suitable for medium and high temperature applications. They are characterized by their ability to directly and efficiently convert the chemical energy of fuel and oxidant into electrical energy under all-solid-state chemical conditions, with minimal environmental impact during the conversion process. They are considered to be the third generation of fuel cells and are highly anticipated in practical applications. They are considered to be the fuel cell closest to the commercialization of proton exchange membrane fuel cells.

(5) A molten carbonate fuel cell is a fuel cell consisting of a porous ceramic cathode, a porous ceramic electrolyte membrane, a porous metal anode, and metal plates. Its electrolyte is molten carbonate. MCFC is a high-temperature battery with an operating temperature of 650-700°C.

(6) A methanol reforming hydrogen fuel cell is a fuel cell system that combines a methanol reforming system with a proton exchange membrane fuel cell stack, using hydrogen-rich reformed gas generated from methanol as fuel. Unlike direct methanol fuel cells, this combined system effectively utilizes the high-efficiency electrical power of the proton exchange membrane fuel cell while also using hydrogen generated by methanol. The amount of hydrogen is determined by the reaction of methanol, so the supply of methanol can be stopped, thereby eliminating the need to consider the storage of excess hydrogen. This reduces production and transportation costs, improves safety, and outperforms direct methanol fuel cells in terms of output power. It is the main focus of future fuel cell technology research and development.

(7) Direct methanol fuel cells (DMFCs) generate electricity directly from methanol-water or steam-methanol reactions, without requiring secondary processing. They are a type of proton exchange membrane fuel cell. Compared to proton exchange membrane fuel cells, DMFCs offer advantages such as rapid start-up at low temperatures, clean fuel, and a simple battery structure, making them suitable for portable electronic devices.

1.2.2 PEMFC structure and working principle

Proton exchange membrane fuel cells (PEMFCs) have become the mainstream fuel cell product on the market due to their high efficiency, rapid start-up at low temperatures, zero pollution, and low noise, with a significant advantage in shipments. A fuel cell stack primarily consists of a catalytic agent, a proton exchange membrane, a gas diffusion layer, and other structural components. A fuel cell stack is primarily constructed from a single fuel cell, each cell comprising a bipolar plate, a sealing ring, and a membrane electrode assembly (MEA). The MEA comprises a proton exchange membrane, a catalytic agent layer, and a gas diffusion layer.

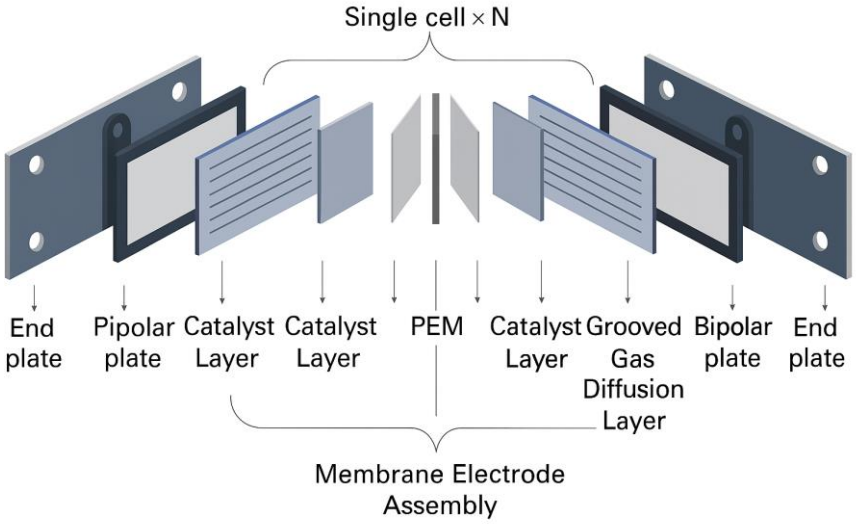

Figure 1.1 Schematic diagram of a typical PEMFC stack structure

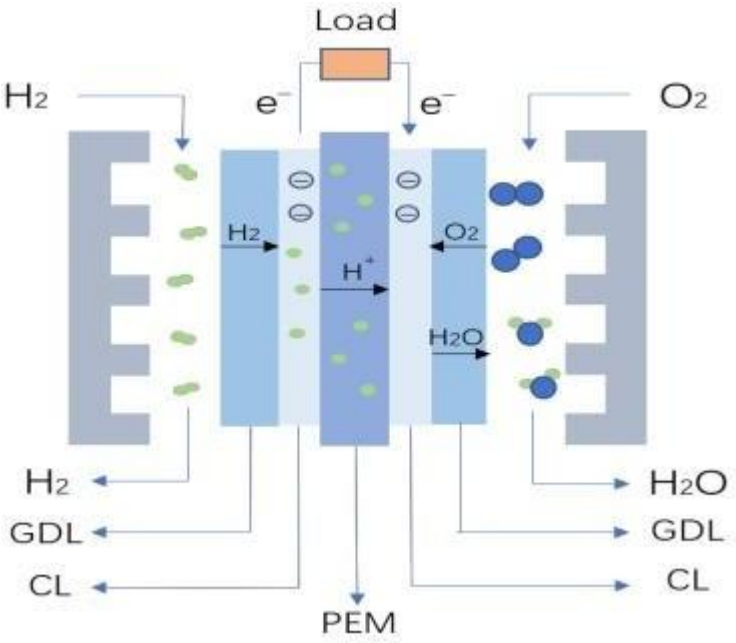

Figure 1.2 Schematic diagram of a single-chip PEMFC stack

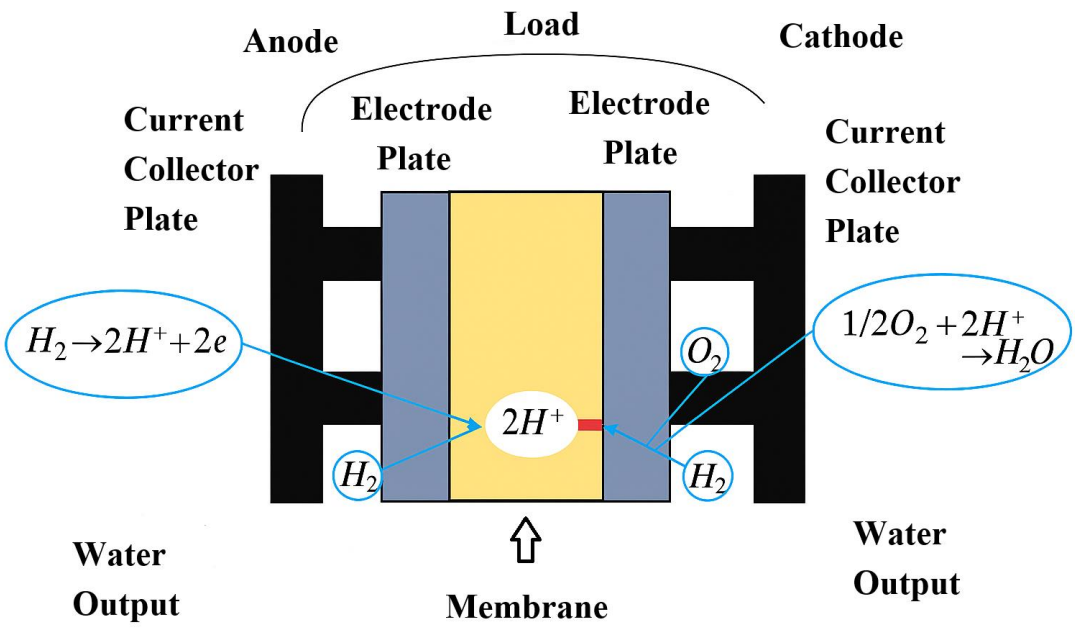

Figure 1.3 Working principle of proton exchange membrane fuel cell

As shown in Figures 1.1, 1.2, and 1.3 above, the operating principle of a proton exchange membrane fuel cell can be summarized as follows: hydrogen in the anode flow channel passes through the gas diffusion layer to the anode electrode, where it reacts with the catalytic agent to produce protons and electrons. The electrons are collected by the current collector and travel through an external circuit to the cathode electrode. The protons pass through the polymer

membrane to the cathode electrode, where they react with the cathode electrons and oxygen from the cathode flow channel to produce the sole reaction product, water. This product water diffuses into the cathode flow channel and then exits the cell through the flow channel.

From the above description of the reaction process, we can see that the cathode flow channel of the fuel cell not only bears the role of supplying reactant oxygen to the ion layer, but also the reaction product water is mainly discharged from the fuel cell through the cathode flow channel. Therefore, the numerical simulation of the single-phase gas flow when the fuel cell is not working to analyze the wind field distribution at the cathode channel has certain reference significance in practical engineering applications.

1.3 Current research status at home and abroad

1.3.1 Current status of wind field simulation research for air-cooled fuel cell systems

There is no research on fuel cell microchannel wind field at home and abroad. At present, scholars focus on the simulation of wind field distribution of atmospheric flow[4][5], typhoon[6], waves[7], terrain[8], etc., and pay attention to the wind field distribution in large space[9], or the simulation analysis of power generation efficiency and heat dissipation effect of heavy wind power equipment such as large generators and turbines[10]. However, there is a lack of research on the unidirectional flow of wind field in a small-scale limited space such as fuel cells. Therefore, this paper chooses the wind field distribution of hydrogen fuel cell microchannel as the starting point to conduct wind field simulation.

1.3.2 Current status of research on performance analysis of air-cooled fuel cell systems

(1) Optimization of fuel cell stack component structure and enhancement of fuel cell stack performance

Many researchers are committed to improving the output performance of the fuel cell stack and optimizing the components of the fuel cell stack, as well as the feasibility of experimental operations. Among them, Gao Weitao et al. [11] conducted a detailed study on the durability and cost-controllable large-scale commercialization of PEMFC. Starting from the research progress and results of the entire industry chain of catalysts, membrane electrode assemblies, fuel cells and fuel cell engines, they sorted out the research hotspots such as single-atom catalysts, non-precious metal catalysts, special morphology catalysts, ordered catalyst layers, high-temperature proton exchange membranes, membrane electrode layer interface optimization, integrated bipolar plate-diffusion layer, and hydrogen system circulation. They concluded that low-platinum/non-

platinum catalyst layers, ultra-thin proton exchange membranes, gradient/ordered membrane electrode assemblies, high-temperature fuel cell operation, and self-humidification are the future development trends, and further innovation and breakthroughs are urgently needed. Xie Yichun et al. [12] conducted a study on the temperature stability control of the proton exchange membrane fuel cell system. When designing the temperature control system of the proton exchange membrane fuel cell, the goal was to meet the heat dissipation requirements under extreme working conditions such as high ambient temperature and high load, and ignored the stability of temperature control under low temperature and low load. In order to improve the stability of the temperature control system for the fuel cell temperature under low ambient temperature and low load, the control strategy was improved on the basis of traditional PID control, which effectively improved the temperature stability of the fuel cell under low environment and low load, thereby effectively enhancing the performance and durability of the fuel cell.

(2) Research on stack water and heat management

In China, Yang Changxing et al. [13] mainly focused on the research status of water thermal management of air-cooled proton exchange membrane fuel cells (PEMFCs). On this basis, they summarized and prospected the important research directions in this field. First, the application background and characteristics of air-cooled PEMFCs were introduced, namely, air-cooled PEMFCs are suitable for low-power, small-mass, and small-volume places; secondly, the current research progress of water thermal management of air-cooled PEMFCs was reviewed, namely, existing research uses experimental and numerical simulation methods to reveal the influence of operating parameters on the thermal management of air-cooled PEMFCs; in addition, by studying the distribution law of liquid water inside air-cooled PEMFCs, its influence on battery performance was revealed. Based on the discovered water thermal management phenomenon, the researchers proposed corresponding optimization measures. By optimizing the flow field structure, the temperature field and humidity field inside the air-cooled PEMFC can be improved; through the new control algorithm, the battery performance is optimized and the battery temperature is kept within a reasonable range. Finally, it is pointed out that studying the dynamic distribution of liquid water in air-cooled PEMFC, analyzing the stress distribution inside the proton exchange membrane, and exploring the attenuation mechanism of the cathode ionizer are important research directions for the hydrothermal management of air-cooled PEMFC. In a review of the simulation analysis of hydrothermal management of fuel cell engines, Dai Liuliang [14] mainly discussed the current research status of hydrothermal management simulation models of proton exchange membrane fuel cells in different dimensions. As an important type of fuel cell, proton exchange membrane fuel cells can be used in automobiles,

small-scale power stations, and portable mobile energy, and are a research hotspot in the current new energy field.

(3) Fuel cell environmental research

In China, Zhang Shengsheng [15] studied the effects of battery catalyzers and sub-zero low-temperature environments on batteries, focusing on the performance and environmental adaptability of key PEMFC materials. The first part mainly focuses on the existing problems in catalyzers, including material screening, preparation process optimization and related tests. The preparation and characterization methods of Pt-based catalyzers such as Pt-Au/C and Pt-Au-TiO2/C were studied, as well as the application effects of tungsten carbide components in catalyzers and catalyzer carriers. The main innovative conclusions are: Pt-Au-TiO2/C catalyzers obtained by chemical reduction method show good CO resistance in electrochemical tests such as cyclic voltammetry; the introduction of tungsten carbide into Pt-based catalyzers can promote the hydrogen desorption oxidation process to a certain extent; in the methanol oxidation process, the addition of tungsten carbide can inhibit the poisoning effect of methanol on the electrode in the low potential region; when tungsten carbide is used as a catalyzer carrier material for PEMFC, it shows excellent antioxidant properties. The research content of PEMFC low temperature environment adaptability mainly includes: the battery tolerance when stored in a sub-zero environment, the performance changes of key components and corresponding solutions, etc., and the impact of the electric drag heating method on the battery was also tested. The results show that when stored in a sub-zero environment, the water in the battery is the direct cause of damage to the electrode structure and performance degradation. Purging the closed battery with inert gas or a small amount of reaction gas can effectively remove most of the water in the flow field and inside the fuel cell, reducing the negative impact of mechanical damage to key components of the battery caused by the freeze-thaw cycle. By monitoring the humidity of the outlet gas, the optimal working point can be determined to ensure the stable working state of the battery; in addition, by reversely pressurizing the PEMFC to promote the flow of proton hydrogen, the battery can be quickly heated. When this method is applied, the factor that has the greatest impact on the heat release is the gas flow rate. This method is expected to be applied to the low-temperature startup process of PEMFC in a sub-zero environment. Yang Zichu [16] conducted an innovative design study of portable hydrogen fuel cells based on field environments, aiming to explore the design research of portable hydrogen fuel cell products in field environments. Methods: Based on portability, practicality, and safety, a total of 8 color combinations and 5 design schemes were designed. Participants were invited to participate in the experiment, and the data was analyzed through eye movement experiments to evaluate the design of portable hydrogen fuel cell products. Among them, the solution with two steel pipes running through the

fuselage has a high degree of freedom of carrying, conforms to the design positioning of military equipment, and can also enhance the firmness of the product, making it the best choice in the experiment. Conclusion: In terms of color design, stable, concealed, and off-road color elements are the best; in terms of interactive design, easy-to-learn and rounded are the most suitable design patterns, which have a certain effect on improving operational efficiency and functional recognition.

1.4 Main research content and technology

1.4.1 Main research content

This paper analyzes the performance and wind field simulation of a 500W fuel cell stack. Compared with water-cooled stacks, air-cooled fuel cells with a small power of about 100W use hydrogen as fuel, a small amount of oxygen in the air as an oxidant to participate in the electrochemical reaction, and excess air is used to cool the stack to keep it working at a certain temperature (not more than 80℃). The use of air cooling technology eliminates the complex and bloated coolant circulation and heat dissipation system (coolant tank, coolant circulation pump, coolant pipe, heat sink, fan, air humidifier, and many sensors, solenoid valves, etc.) in liquid cooling technology, and also eliminates the bulky and high-power air compressor (which consumes 20-40% of the fuel cell power generation during normal operation), making the entire system simple, easy to operate and control. Because it does not have a cooling water system and complex air intake pipes, and does not require a water storage device, it has incomparable advantages in terms of size and portability [17][18]. Therefore, it is generally considered to be an ideal power source for portable power supplies and unmanned aerial vehicles (UAVs).

In air-cooled fuel cells, the cathode channel is open. To maintain stable battery operation, a large amount of air is used for cooling. When the air is blown at a high velocity onto the cathode surface, it will carry away the water generated by the electrochemical reaction, leaving the proton exchange membrane in a dry state. This will increase the membrane resistance, further causing the battery temperature to rise. If the temperature is further reduced by increasing the air volume, the entire process will fall into a vicious cycle. To solve this problem, people usually use self-humidifying membranes prepared by modifying silica or other materials, or perform humidification and water retention treatment on the electrode layer of the membrane electrode, so that the water generated by the electrochemical reaction can be retained on the cathode side, reaching a membrane wetting state.

1.4.2 Technical route

At present, the performance analysis of air-cooled fuel cells at home and abroad is not in-depth enough. The author conducted experiments based on the 500W fuel cell test bench built by

Zhang Jiekai under different working conditions [19], and obtained the temperature, single voltage, and electric power of the fuel cell. Based on this, Matlab was used to draw a two-dimensional curve graph according to the specific experimental data, and the fuel cell performance analysis was carried out. As for the wind field simulation, SolidWorks software was used to build a three-dimensional model according to the actual proportion, ICEM CFD was used to divide the grid into blocks, and the grid size of different precisions was set accordingly. Fluent was imported, the inlet and outlet parameters were set, and the grid was solved. After that, Tecplot software was used for post-processing to study the wind field distribution in the X, Y, and Z directions, and the wind field streamline diagram in the Z direction, which is parallel to the microchannel flow direction, was mainly analyzed. The inlet wind speed was changed, four cases were set and analyzed. As for the analysis of fuel cell performance, the working conditions were changed according to the specific experiment to carry out specific measurements.

2. Mathematical Models and Numerical Methods

2.1 Model assumptions

2.1.1 Model construction principles

As shown in Figures 2.1, 2.2, 2.3, and 2.4, this paper approximates the modeling and simulation based on the actual size of the fuel cell, simplifying the wind field simulation inside the fuel cell into a physical object composed of multiple structures [20]. Air enters the stack from a small cylinder on one side and flows out from four large cylinders arranged side by side on the other side. The large cylinders represent four DELTA fans with a size of 30*30*25.4mm. The model is a fan-suction fluid flow at the outlet, simulating the wind field simulation of the fluid domain inside the stack when the stack is not running. The fluid medium is single-phase air flow, the inlet is natural convection, the pressure is one standard atmospheric pressure, and the remaining walls are the inner walls of the physical object.

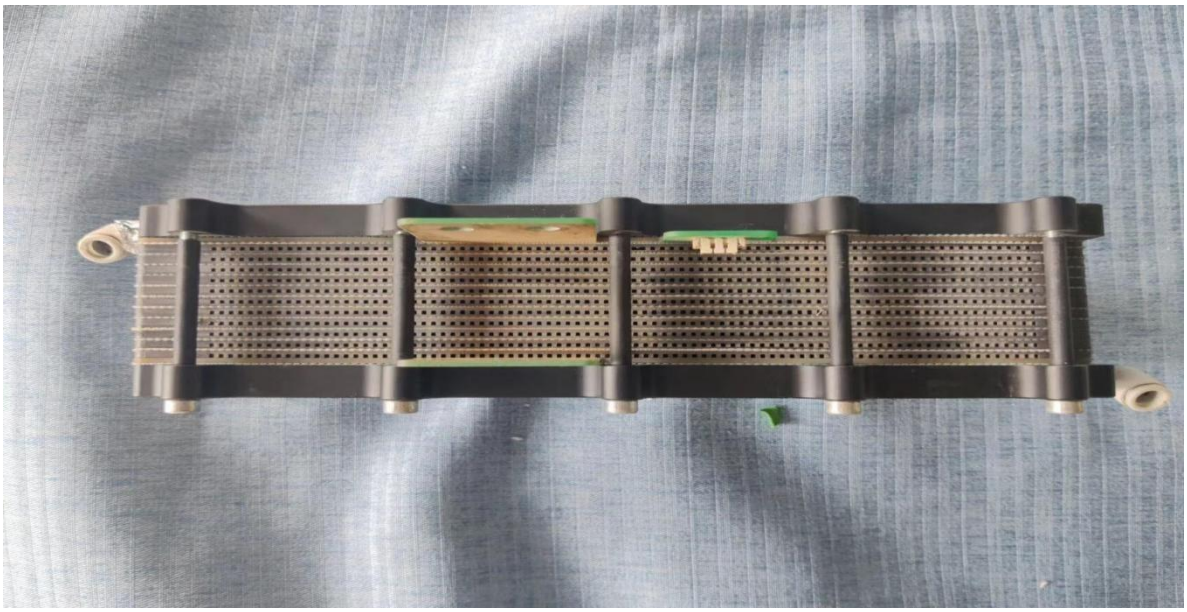

Figure 2.1 Fuel cell microchannel front view

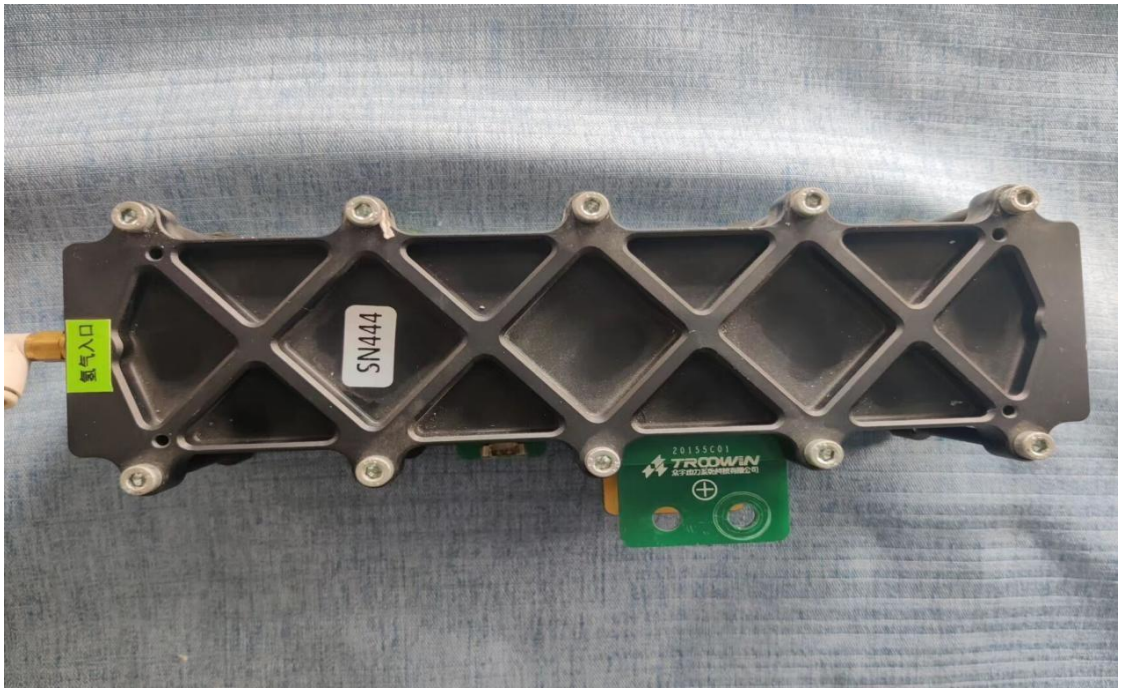

Figure 2.2 Fuel cell microchannel back view

Figure 2.3 Front view of the outlet of the fuel cell and fan

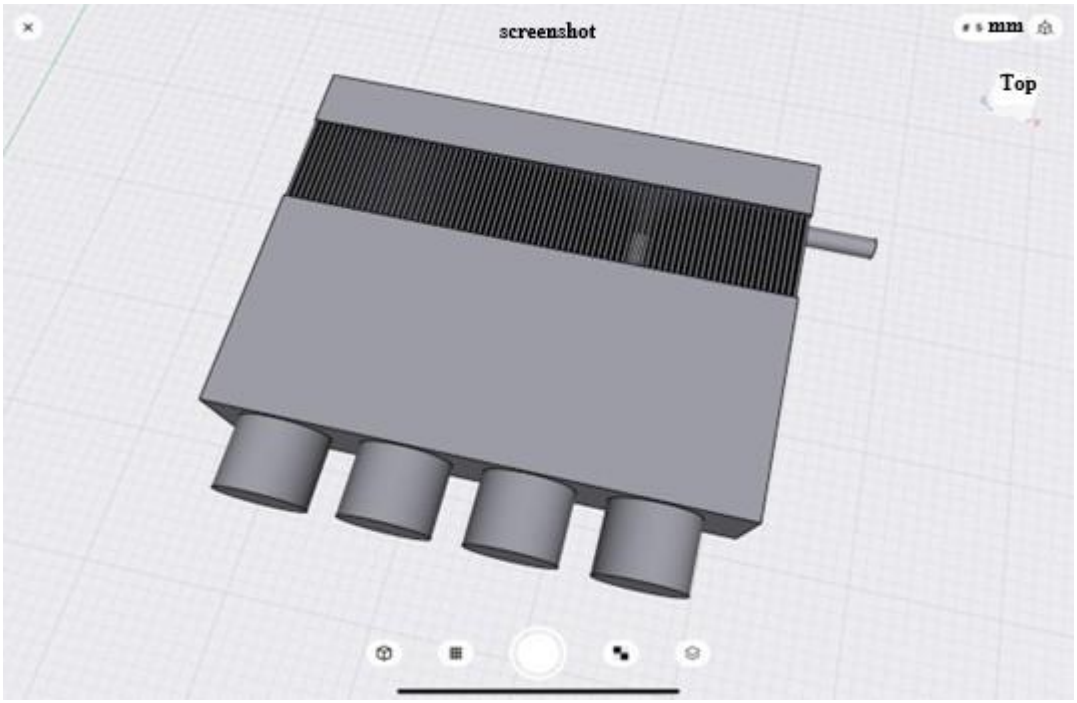

Figure 2.4 Top view of the fuel cell system fluid domain model based on the physical approximation

2.1.2 Model specific dimensions and fan equipment specific parameters

Taking into account the actual simulation accuracy requirements and the numerical computational workload after meshing, the inlet was set to 8mm in diameter and 30mm in height. The dimensions of the rectangular block connecting the inlet were set to 172mm*20.564mm*36.9mm in length, width, and height. The microchannels were arranged in an 86*11 pattern, with each microchannel measuring 1mm*1mm. The spacing between microchannels was 1mm along the length and 2.2mm along the height. The rectangular block connecting the outlet measured 172mm*78.436mm*35.705mm, and the outlet contained four Delta fans measuring 30mm*30mm*25.4mm in length and width.

The fan is a DC power supply, and the fan speed is adjusted according to the voltage. The dimensions of the model may differ from the actual manufacturer, but due to the approximate simulation, the wind speed selection is still determined by the fan parameters of 60mm*60mm*25.4mm. The fan performance parameters and the corresponding relationship between fan voltage and wind speed are shown in Figure 2.5 and Table 2.1.

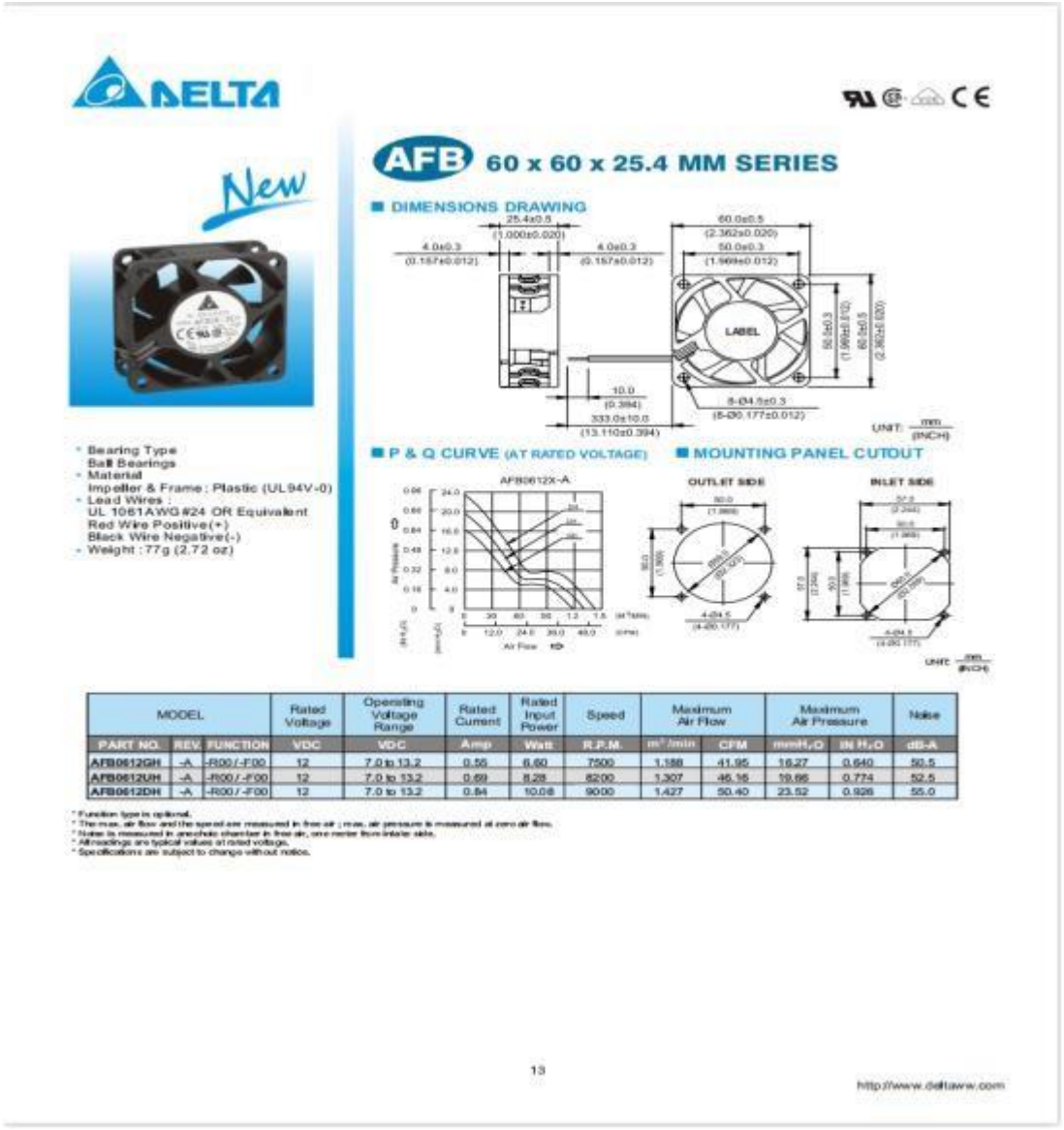

MODEL			Rated Voltage	Operating Voltage Range	Rated Current	Rated Input Power	Speed	Maximum Air Flow		Maximum Air Pressure		Noise
PART NO.	REV.	FUNCTION	VDC	VDC	Amp	Watt	R.P.M.	m^3/min	CFM	mmH_2O	IN H_2O	dB-A
AFB0612GH	-A	-R00 / -F00	12	7.0 to 13.2	0.55	6.60	7500	1.188	41.95	16.27	0.640	50.5
AFB0612UH	-A	-R00 / -F00	12	7.0 to 13.2	0.69	8.28	8200	1.307	46.16	19.66	0.774	52.5
AFB0612DH	-A	-R00 / -F00	12	7.0 to 13.2	0.84	10.08	9000	1.427	50.40	23.52	0.926	55.0

Figure 2.5 Manufacturer's performance parameters of outlet fans

Table 2.1 Corresponding relationship between fan voltage and air flow rate in actual working conditions

Fan voltage (V)	5	6	8	10	11	12	13.8
Air flow rate (m/s)	1.26	1.54	2.11	2.83	3.19	3.6	4.35
Air flow (m^3/s)	0.014	0.017	0.023	0.031	0.035	0.039	0.047

2.1.3 Model assumptions

Regarding the flow process of air in the flow channel of a proton exchange membrane fuel cell, the following assumptions are made while ensuring the accuracy of the model as much as possible [21][22]:

(1) After simulation, the Reynolds number at the fuel cell outlet is always kept above 2000, which is significantly higher than the critical state. Therefore, it is assumed that the flow in the flow channel is always turbulent;

(2) Consider the flow of gas in the flow channel, assuming it is an incompressible fluid;

(3) Without considering the reaction of the battery stack, the model only analyzes the changes in the wind field;

(4) Usually the air in the cathode flow channel is saturated, so the phase change of the air can be ignored;

(5) Ignore the roughness of the porous medium surface in the flow channel, assume it is a flat surface, and ignore the material and energy exchange on each surface of the flow channel;

(6) The influence of buoyancy is small in this simulation, so the influence of gravity on wind field distribution is ignored in this paper.

2.2 Research methods

Starting from analyzing the motion of the fluid at each fixed point in the space occupied by the fluid, that is, setting up an observation station to study the motion of the fluid in the entire space, this is called the Euler method. The Euler method studies the motion of fluid, and its focus is on the spatial point in the flow field or the control volume. That is, it studies the changes in the velocity, pressure, density and other physical quantities of the fluid at a fixed spatial point in the space occupied by the moving fluid over time.

2.3 Governing equations

This paper uses the Euler method to analyze the flow of air medium in the fluid domain inside the fuel cell. The equations used are the continuity equation and the momentum equation [23].

2.3.1 Continuity equation

All flow problems must comply with the law of conservation of mass, that is, the mass flowing into the control surface per unit time is equal to the sum of the mass increment of the control body per unit time and the mass of the fluid flowing out of the control body, thus obtaining the following equations (2-1) and (2-2):

$$\frac{\partial \rho}{\partial t}+\frac{\partial(\rho u)}{\partial x}+\frac{\partial(\rho v)}{\partial y}+\frac{\partial(\rho w)}{\partial z}=0 \qquad (2-1)$$

For a continuous incompressible fluid, the density is a constant:

$$\frac{\partial \rho}{\partial t} + \nabla \cdot (\rho V) = 0 \qquad (2-2)$$

Where: ρ is density, t is time, V is velocity vector in each direction, u, v, and w are velocity vectors in the x, y, and z directions respectively.

2.3.2 Momentum conservation equation

All flow systems must comply with the basic law of momentum conservation. That is, the sum of the various external forces on the microelement is equal to the rate of change of the fluid momentum in all the control microelement with respect to time, which can be expressed mathematically as follows (2-3):

$$\delta_F = \delta_m \frac{dv}{dt} \qquad (2-3)$$

The momentum conservation equation is obtained in the rectangular coordinate system based on the viscous constitutive equation of the fluid, namely the N-S equation, as shown in equations (2-4), (2-5), and (2-6):

$$\rho \frac{du}{dt} = \rho F_x - \frac{\partial p}{\partial x} + \frac{\partial}{\partial x}\left(\mu \frac{\partial u}{\partial x}\right) + \frac{\partial}{\partial y}\left(\mu \frac{\partial u}{\partial y}\right) + \frac{\partial}{\partial z}\left(\mu \frac{\partial u}{\partial z}\right) + \frac{\partial}{\partial x}\left[\frac{\mu}{3}\left(\frac{\partial u}{\partial x} + \frac{\partial v}{\partial y} + \frac{\partial w}{\partial z}\right)\right] \qquad (2-4)$$

$$\rho \frac{dv}{dt} = \rho F_y - \frac{\partial p}{\partial y} + \frac{\partial}{\partial x}\left(\mu \frac{\partial v}{\partial x}\right) + \frac{\partial}{\partial y}\left(\mu \frac{\partial v}{\partial y}\right) + \frac{\partial}{\partial z}\left(\mu \frac{\partial v}{\partial z}\right) + \frac{\partial}{\partial y}\left[\frac{\mu}{3}\left(\frac{\partial u}{\partial x} + \frac{\partial v}{\partial y} + \frac{\partial w}{\partial z}\right)\right] \qquad (2-5)$$

$$\rho \frac{dw}{dt} = \rho F_z - \frac{\partial p}{\partial z} + \frac{\partial}{\partial x}\left(\mu \frac{\partial w}{\partial x}\right) + \frac{\partial}{\partial y}\left(\mu \frac{\partial w}{\partial y}\right) + \frac{\partial}{\partial z}\left(\mu \frac{\partial w}{\partial z}\right) + \frac{\partial}{\partial z}\left[\frac{\mu}{3}\left(\frac{\partial u}{\partial x} + \frac{\partial v}{\partial y} + \frac{\partial w}{\partial z}\right)\right] \qquad (2-6)$$

2.4 Meshing

2.4.1 Grid division ideas

The fluid calculation domain is a relatively fine and distinctive small-scale space body. This paper comprehensively considers the accuracy of numerical simulation and the computational cost of the number of grids, implements overall modeling, and focuses on analyzing the wind field distribution of the longitudinal section of the microchannel and the streamline distribution of the cross section of the model. Although the overall model is relatively complex, according to the focus of the research topic [24][25], it is only necessary to divide the whole into five parts and set different grid sizes for each part. In this way, the number of grids can be appropriately reduced while ensuring the calculation accuracy, thereby improving the calculation efficiency.

2.4.2 Grid specific condition settings

As shown in Figures 2.6 and 2.7, the corresponding volume mesh and surface mesh data are set, the mesh is generated, and the mesh quantity and quality are tested. As shown in Figures 2.8 and 2.9, the test shows that the mesh quantity and quality can meet the accuracy required for the study.

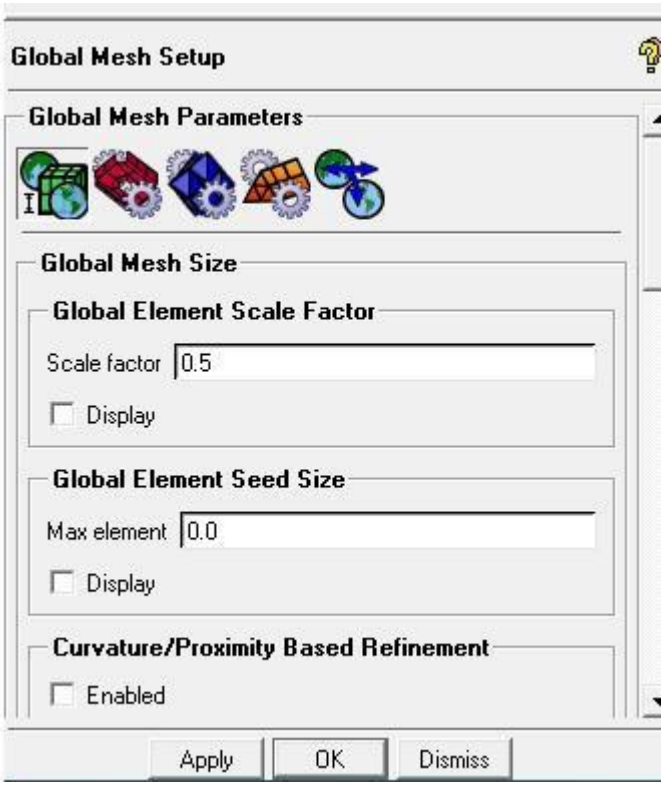

Figure 2.6 Volume mesh setting parameters in ICEM CFD

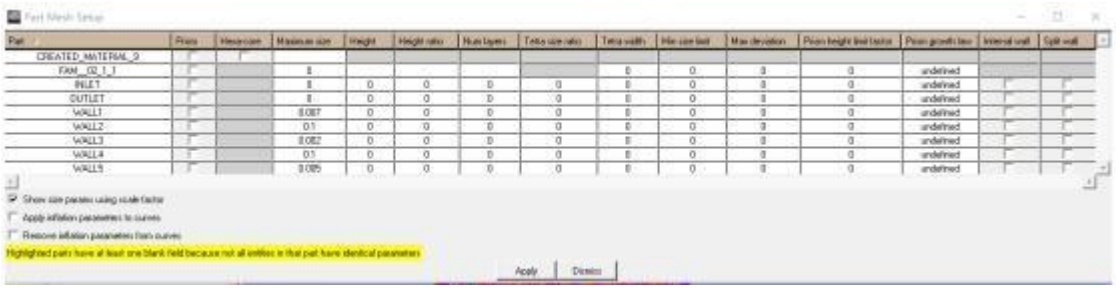

Figure 2.7 ICEM CFD mid-surface mesh setting parameters

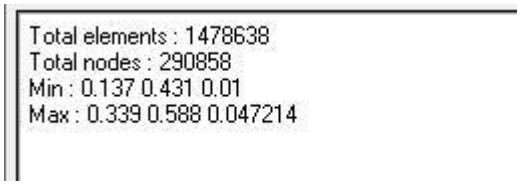

Figure 2.8 Data on the number of meshes and the maximum and minimum mesh sizes in ICEM CFD

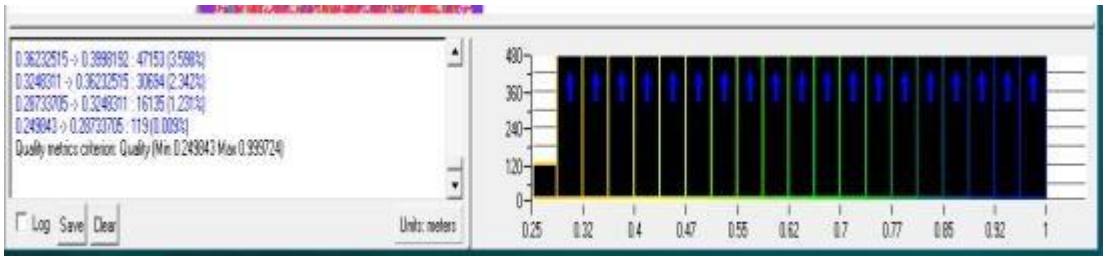

Figure 2.9 Mesh quality in ICEM CFD

As shown in Figures 2.10, 2.11, 2.12, and 2.13, the top view of the overall mesh, the mesh generation at the fluid domain air inlet, fan outlet, and micro-passage are shown in detail and intuitively.

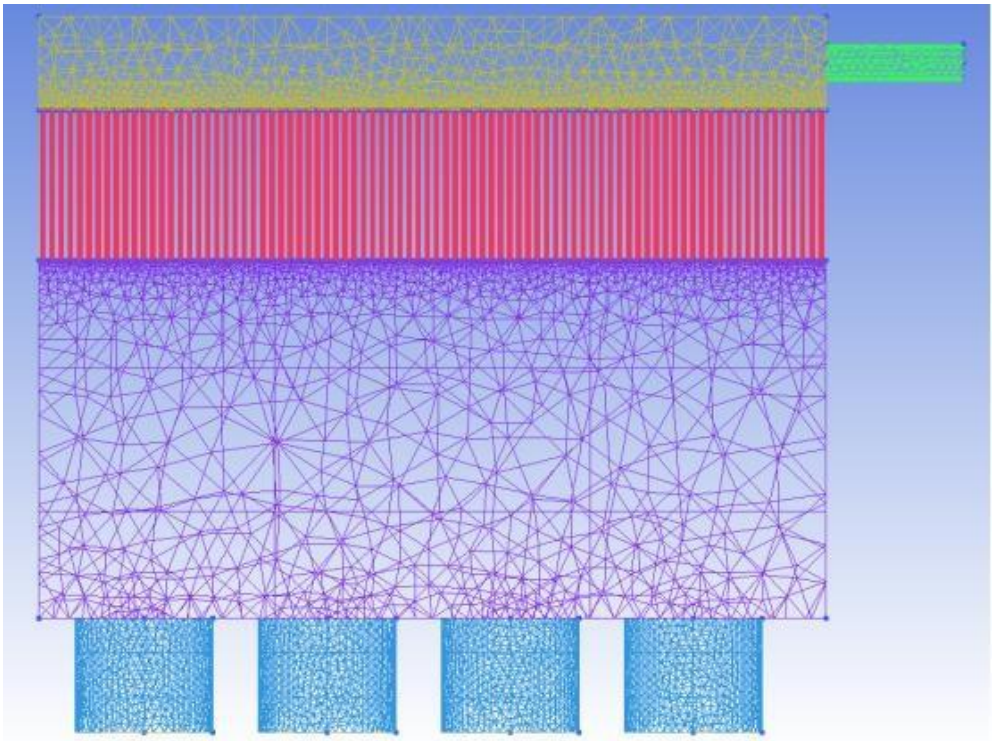

Figure 2.10 Mesh generation diagram in ICEM CFD

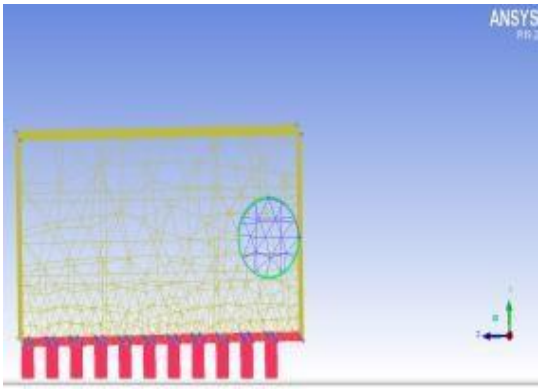

Figure 2.11 Partial view of the grid at the inlet side

Figure 2.12 Partial view of the grid at the microchannel

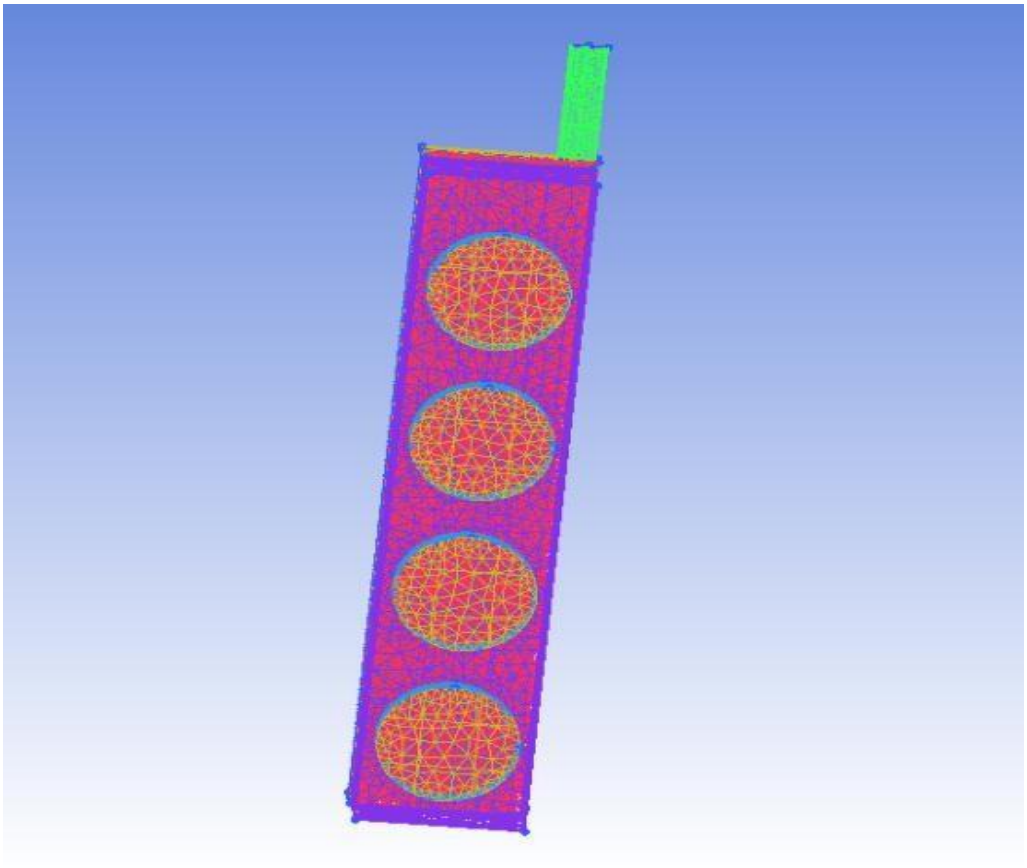

Figure 2.13 Partial view of the outlet side grid

2.5 Grid independence verification

To ensure the accuracy of the Fluent simulation and consider computing resources, the outlet wind speed is set to 3.6 m/s in the boundary conditions, as the wind field distribution perpendicular to the Z axis of the fuel cell system is relatively regular when the outlet wind speed is 3.6 m/s. Fluent simulations were performed at mesh sizes of 1.4 million, 2 million, and 4 million. Significant differences were observed between the Fluent calculation results for the 1.4 million and 4 million mesh sizes, and the results obtained with the 4 million mesh size iterative solution differed significantly from the actual results. However, the results obtained with the 1.4 million and 2 million mesh sizes were nearly identical, as shown in Figures 2.14 and 2.15. Therefore, the 1.4 million mesh size was adopted as the standard mesh size. The convergence of the 1.4 million mesh size after 5000 iterations is shown in Figure 2.16, demonstrating good results.

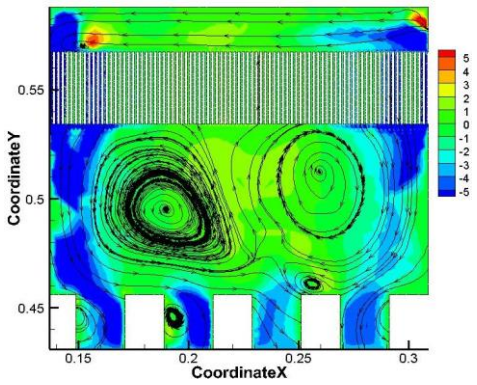

Figure 2.14 Top view of a 1.4 million grid wind field simulation

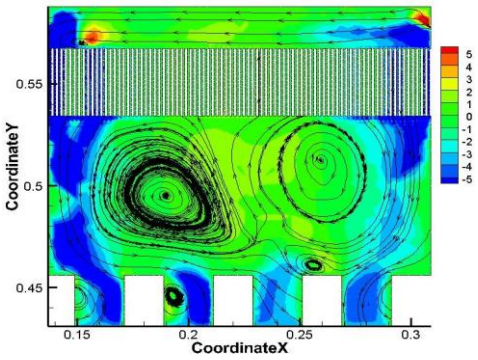

Figure 2.15 Top view of a 2 million grid wind field simulation

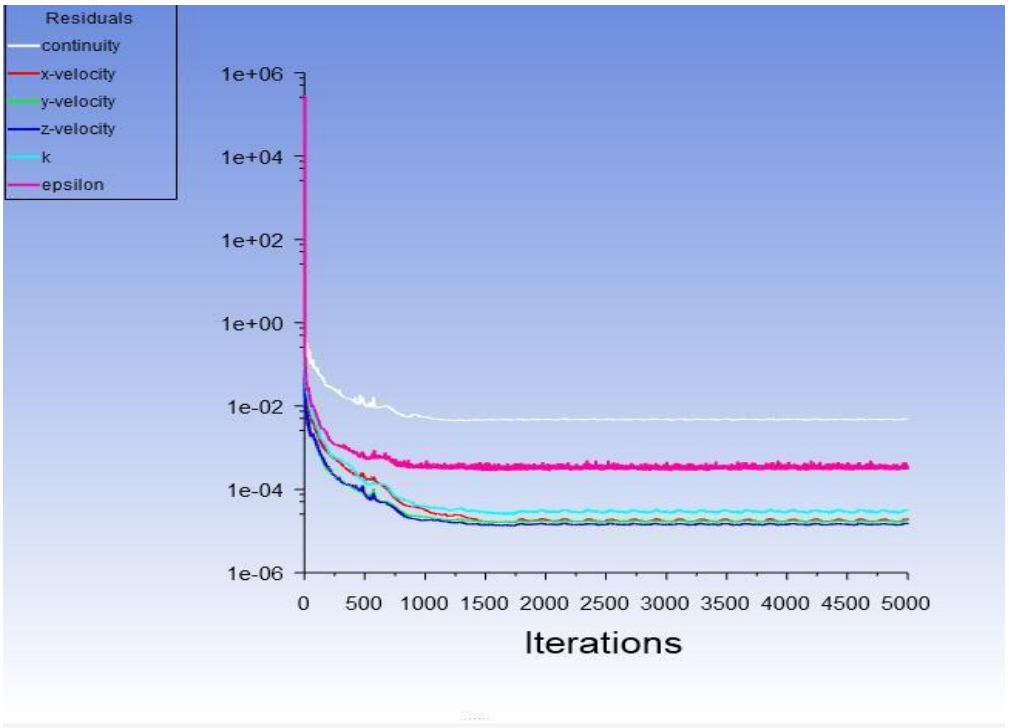

Figure 2.16 Convergence of the grid after 5,000 iterations

3. Wind field distribution inside the fuel cell system when the stack is not running

By calculating the Reynolds number at the outlet, we determined that the fluid domain was turbulent. Therefore, we selected the k-epsilon model in Fluent. The inlet was set to pressure-inlet, with the pressure set to 101325 Pa, and the outlet was set to velocity-inlet. Since the fan is a suction exhaust, the outlet velocity value was negatively signed based on the actual operating conditions to indicate the direction of the exhaust. The remaining fluid domain boundary conditions were set to no slip by default, with no specific settings. The number of arrival steps was set to 5000, and finally, the corresponding reference data was set for simulation. This chapter's wind field simulation focuses on the wind field distribution in the fuel cell system fluid domain under different fan outlet wind speeds.

3.1 Working condition settings

The geometric model is shown in Figure 3.1. The boundary conditions of the model are: the flow channel inlet is the pressure inlet, the flow channel outlet is the fan outlet, the inlet pressure is constant at Pout = 1atm, and wall1, wall2, wall3, wall4, and wall5 are fixed no-slip walls.

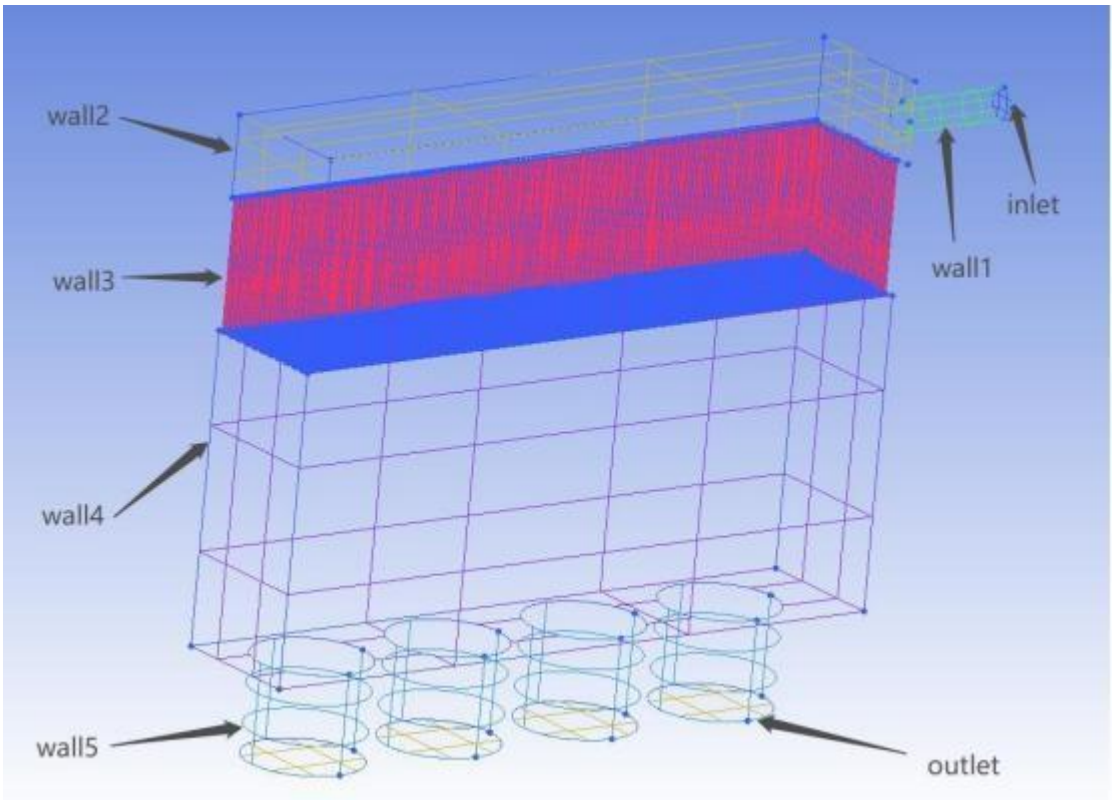

Figure 3.1 Schematic diagram of model area division

The fan speed is selected based on the manufacturer's parameters, that is, the outlet wind speed is determined by the fan voltage. As shown in Table 3.1 below, the fan voltages are

selected as 12V, 11V, 10V, and 8V, corresponding to fan speeds of 3.6m/s, 3.19m/s, 2.83m/s, and 2.11m/s. Therefore, this chapter selects the above four different outlet wind speeds for wind field simulation and analyzes the corresponding four results.

Table 3.1 Relationship between fan voltage and wind speed

Fan voltage (V)	5	6	8	10	11	12	13.8
Air flow rate (m/s)	1.26	1.54	2.11	2.83	3.19	3.6	4.35
Air flow (m^3/s)	0.014	0.017	0.023	0.031	0.035	0.039	0.047

Following the above steps, the grid was solved using Fluent software. The flow field distribution solutions for fan voltages of 8V, 10V, 11V, and 12V were obtained, corresponding to fan speeds of 2.11m/s, 2.83m/s, 3.19m/s, and 3.6m/s. Further refinement and post-processing using Tecplot software yielded the wind field distribution perpendicular to the Z direction and streamline wind direction diagrams shown in Figures 3.2, 3.3, 3.4, and 3.5.

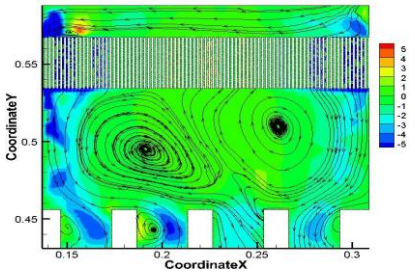

Figure 3.2 Top view of wind field with wind speed of 2.11m/s

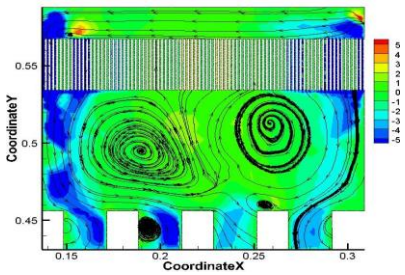

Figure 3.3 Top view of wind field with wind speed of 2.83m/s

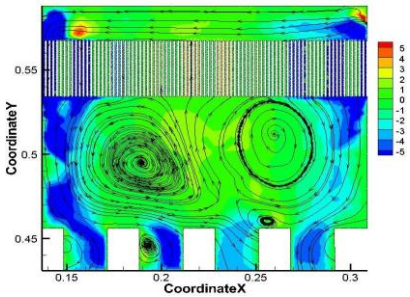

Figure 3.2 Top view of wind field with wind speed of 3.19m/s

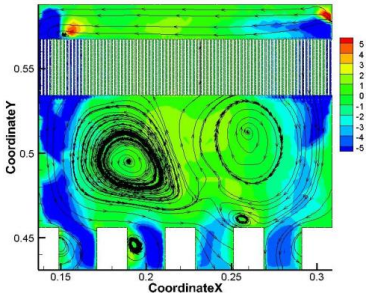

Figure 3.3 Top view of wind field with wind speed of 3.6m/s

Combined with Figures 3.2, 3.3, 3.4, and 3.5 above, we can see that as the fan speed increases, the wind speed near the model outlet increases significantly, especially the influence range of the vortex at the fan is expanding. Similarly, the wind field at the air inlet gradually becomes stable from the initial turbulence. As shown in the figure, we can find that in the fluid domain of the fuel cell system, the wind direction near the two side walls is flowing toward the fan outlet, and the flow field is relatively continuous. The backflow effect at the corners of the wall along the way does not have too much influence. In contrast, the wind field in the middle of the fluid domain is more complex and dense. Two large vortices appear in the middle area. Under the interaction of the vortices, part of the wind field in the middle area flows toward the fan outlet, and part flows back to the microchannel wall, partly strengthening and partly weakening the fluid flow at the intersection of the microchannel and the wall.

The vortex at the fan outlet can be explained by Bernoulli's principle [26], as shown in Figure 3.6. When the fan is actually running, the wind field near the fan is not a long straight space with the same area as the blade area, but there is a period of free development until the wind field is completely stable. According to the model established based on the physical approximation, the volume of the fluid domain that contacts the fan, that is, the volume represented by wall5, is a cylinder with the same area as the fan. Therefore, the wind field caused by the pressure drop at the fan is in a restricted motion in the section extending to the outlet wall and the section connected to wall4. Therefore, the backflow on the pipe wall causes a vortex, which increases the wind speed of a part of the wind field at the outlet.

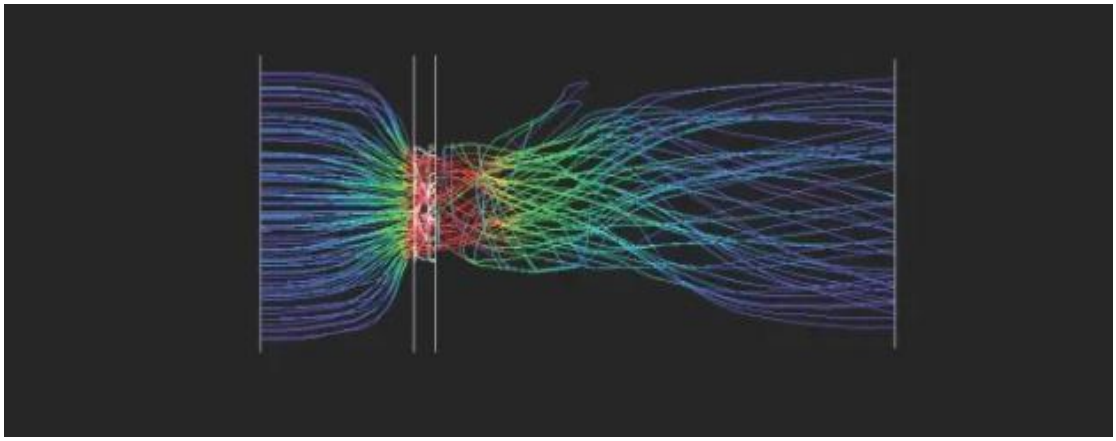

Figure 3.6 Schematic diagram of spiral airflow distribution at the fan

Following the above steps, the grid was solved using Fluent software. The flow field distribution solutions for fan voltages of 8V, 10V, 11V, and 12V were obtained for fan speeds of 2.11m/s, 2.83m/s, 3.19m/s, and 3.6m/s, respectively. Further refinement and post-processing

using Tecplot software yielded the wind field distributions perpendicular to the Y direction in the microchannel, as shown in Figures 3.7, 3.8, 3.9, and 3.10.

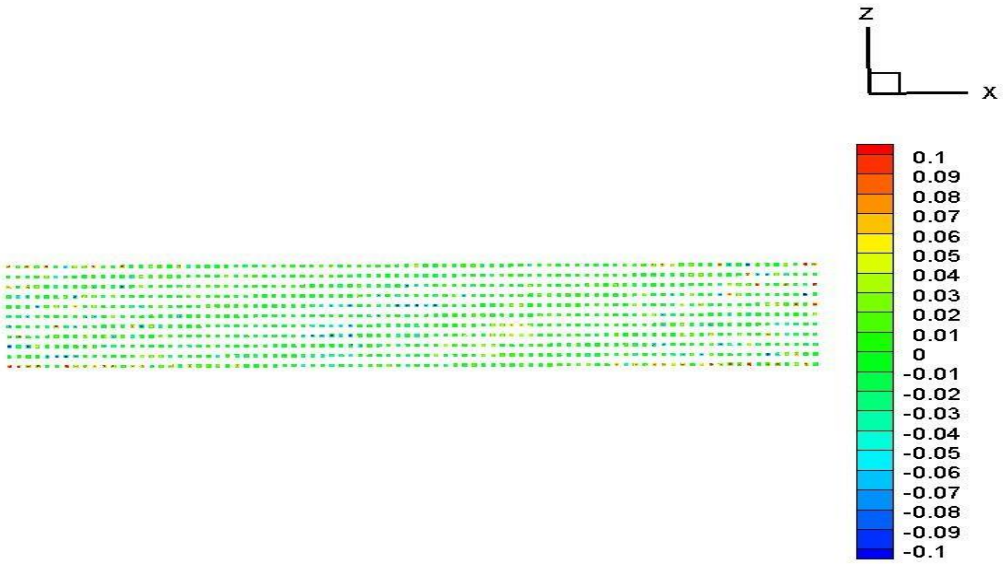

Figure 3.7 Wind field distribution in the microchannel when the fan speed is 2.11m/s

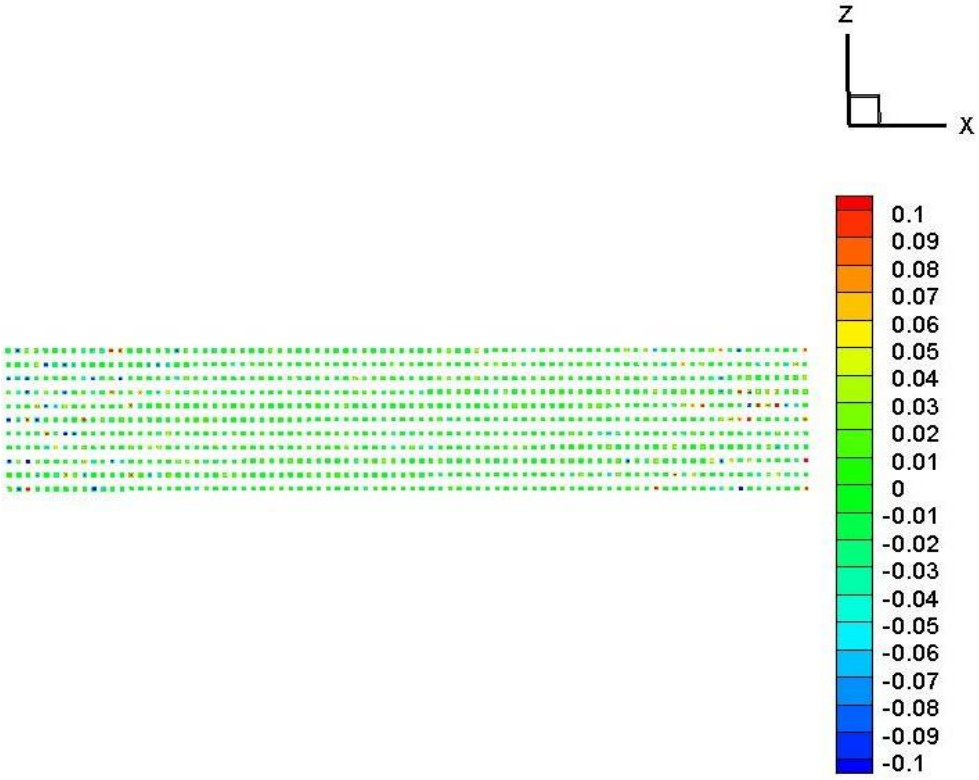

Figure 3.8 Wind field distribution in the microchannel when the fan speed is 2.83m/s

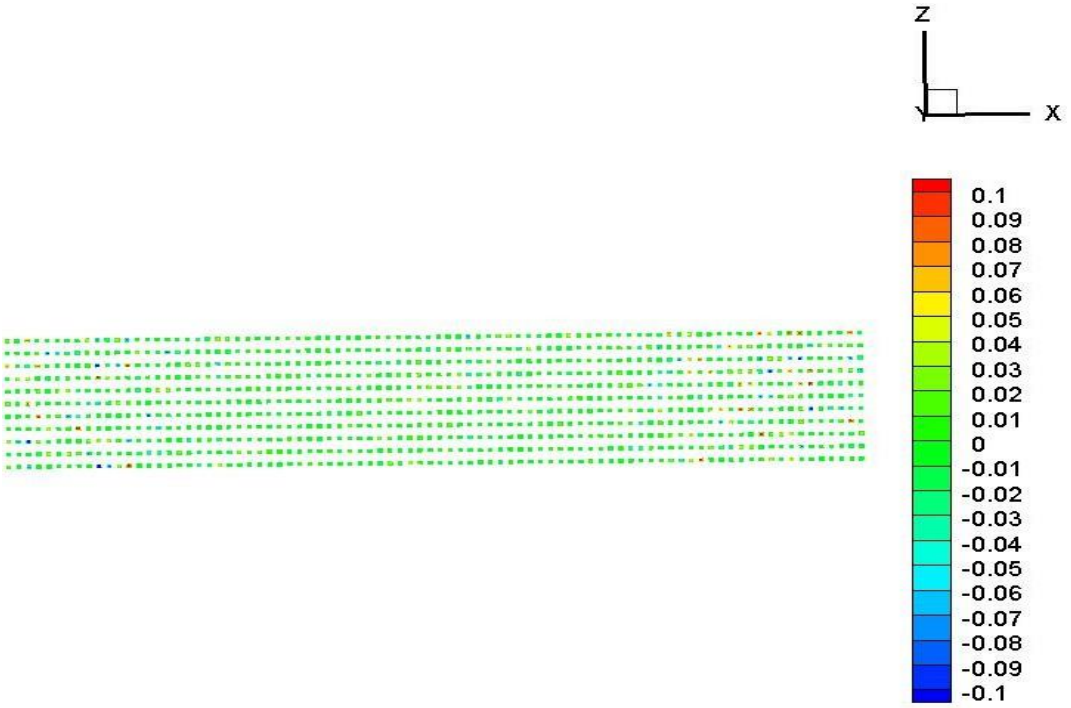

Figure 3.9 Wind field distribution in the microchannel when the fan speed is 3.19m/s

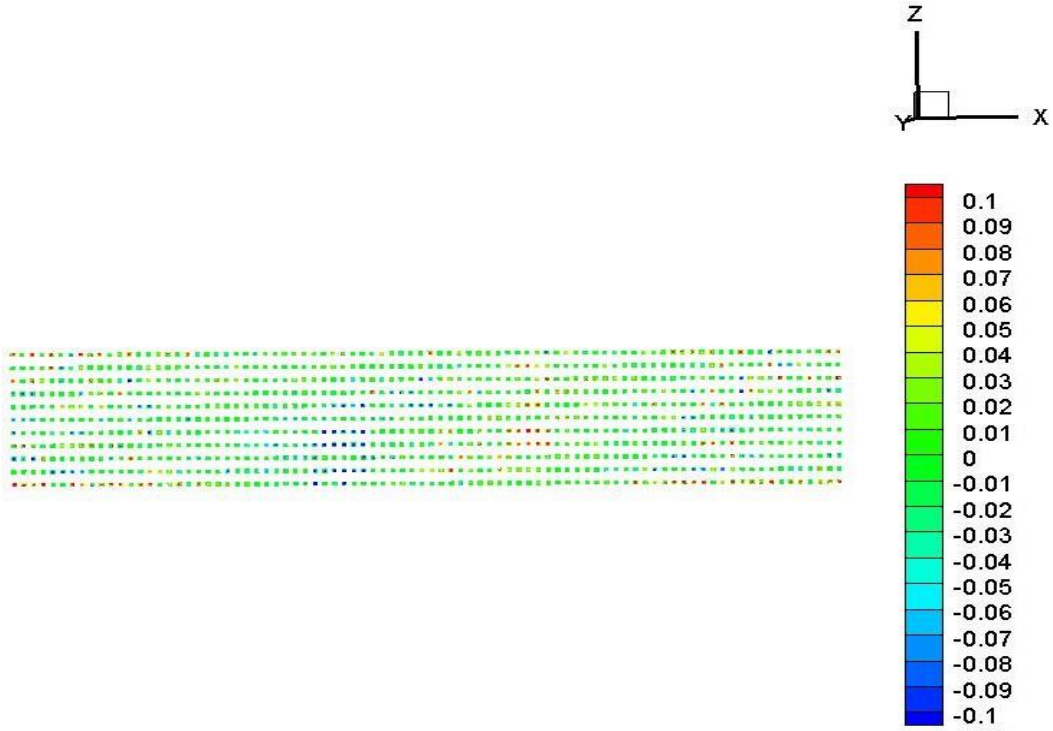

Figure 3.10 Wind field distribution in the microchannel when the fan speed is 3.6m/s

Combined with Figures 3.7, 3.8, 3.9, and 3.10 above, it is found that the disturbance near the fluid domain boundary on both sides of the microchannel is enhanced with the increase of the

fan wind speed at the outlet, and there is obvious backflow. Its distribution is consistent with the analysis in the previous section. In contrast, the wind field in the middle of the microchannel is further enhanced with the increase of the outlet wind speed. The intensified backflow effect further strengthens the suction speed of the air fluid.

4. Performance Analysis of Air-Cooled Fuel Cell Systems

The performance analysis of air-cooled fuel cell systems[27] mainly involves recording relevant physical quantities through experiments on real fuel cells, and then post-processing the experimental data through Matlab to draw a two-dimensional graph.

Figure 4.1 Fuel cell experimental platform[19]

As shown in Figure 4.1 above, the experimental setup utilizes the fuel cell platform built by Zhang Jikai. The stack used in the experiment is a self-humidifying cathode open proton exchange membrane fuel cell stack consisting of 10 single cells. The stack parameters are shown in Figure 4.2. In addition, three axial flow fans (DELTA, AFB0612GH) with dimensions of 60*60*25.4mm and an operating voltage range of 5-13.8V were placed in parallel at the cathode air outlet (in "intake" mode). These fans supplied the stack with air required for the reaction, cooled the stack, and discharged the product water generated by the fuel cell reaction within the cathode channel.

Parameter	Value	Unit
Dimensions	200×60×60(L*W*H)	mm
Weight	1038	g
Single Cell Quantity	10	cm^2
Single Cell Active Area	65	—
Hydrogen Inlet Pressure	0.05-0.1	MPa
Hydrogen Purity	≥99.95%	W
Rated Power	180	A
Rated Operating Temperature	55	℃
Rated Purge Period	20/0.2	s
Start-up Time	≤5	s

Figure 4.2 Basic parameters and operating conditions of the experimental stack[19]

The experimental data was recorded using the measurement and control platform developed by Zhang Jikai. Its control interface is shown in Figure 4.3.

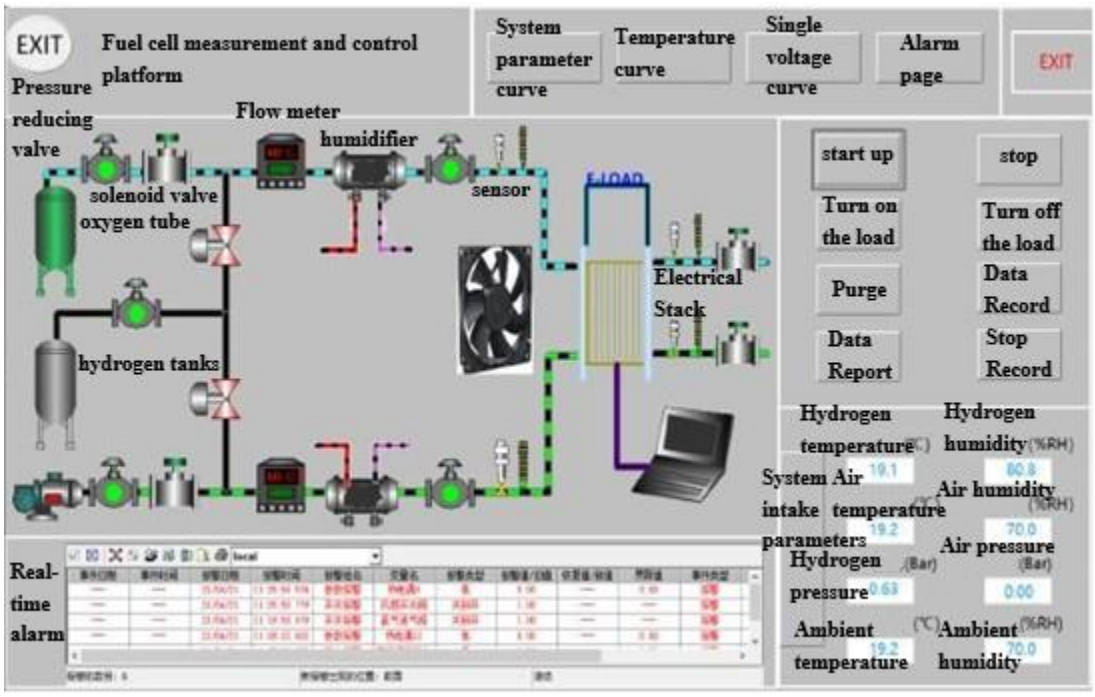

Figure 4.3 Main interface of host computer control and monitoring[19]

When changing the working conditions to conduct experiments and recording data, the platform interface is as shown in Figure 4.4, so that the experimenter can monitor the experimental status in real time.

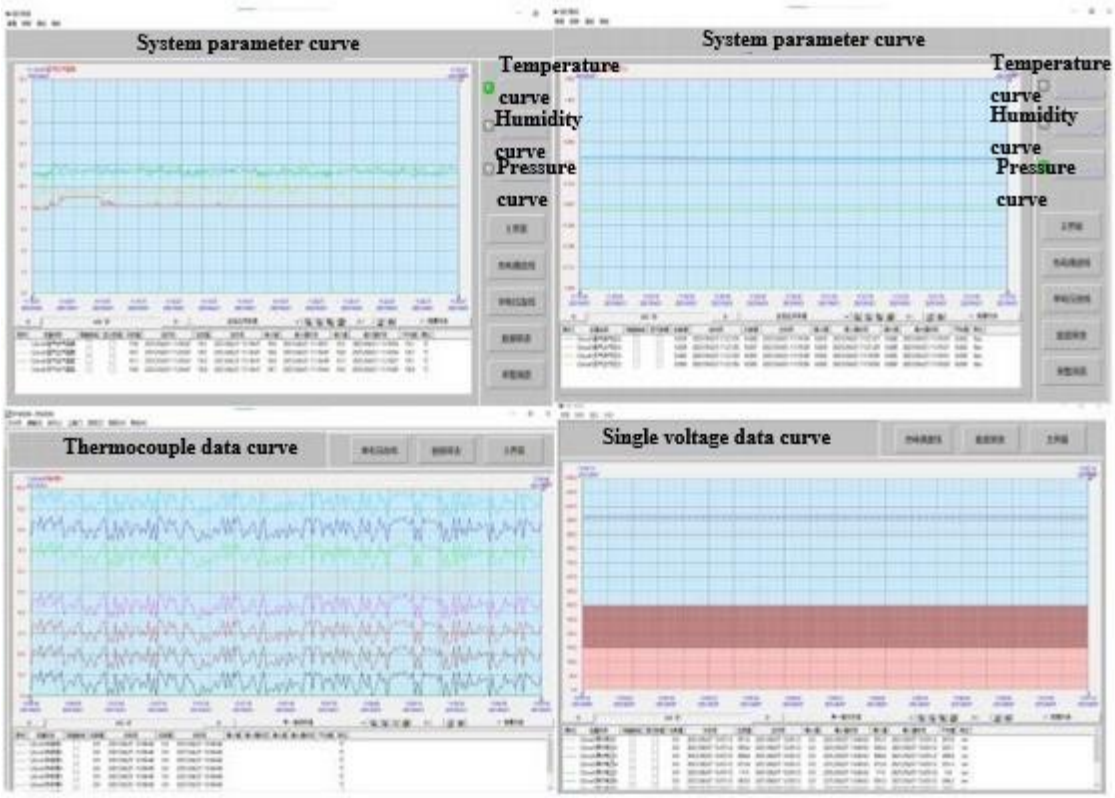

Figure 4.4 Real-time parameter curve interface of the host computer[19]

After each experiment, data is recorded and output through the data report interface. The data report can display the parameter data of the system during operation, record and count the data, and is an indispensable section. It can not only reflect the real-time status of the collected data, but also store, count and analyze long-term data, allowing operators to understand and analyze the relevant status of the system. The upper computer data report and interface in this article are shown in Figure 4.5. This interface can read and query the real-time and historical data of the measurement and control platform and provide functions such as report saving and historical data query.

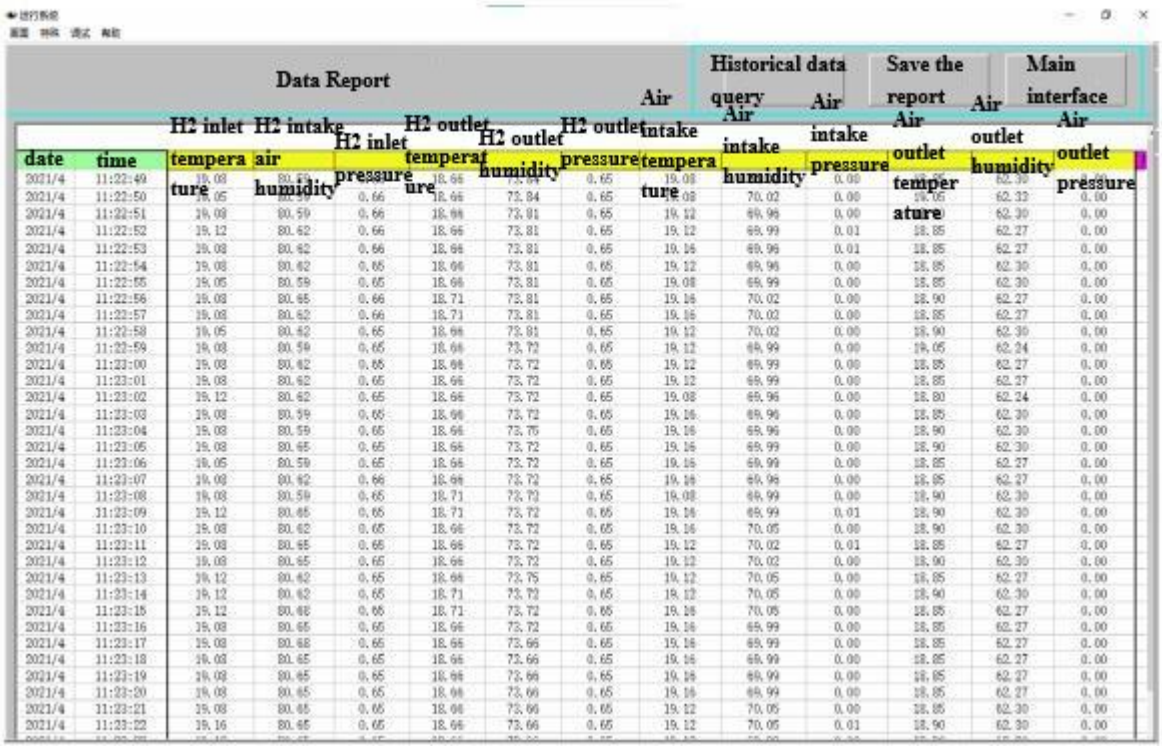

date	time	H2 inlet temperature	H2 intake air humidity	H2 inlet pressure	H2 outlet temperature	H2 outlet humidity	H2 outlet pressure	Air intake temperature	Air intake humidity	Air intake pressure	Air outlet temperature	Air outlet humidity	Air outlet pressure
2021/4	11:22:49	19.08	80.59	0.66	18.66	73.84	0.65	19.08	70.02	0.00	18.85	62.30	0.00
2021/4	11:22:50	19.05	80.59	0.66	18.66	73.84	0.65	19.08	70.02	0.00	18.85	62.30	0.00
2021/4	11:22:51	19.08	80.59	0.66	18.66	73.81	0.65	19.12	69.96	0.00	18.85	62.30	0.00
2021/4	11:22:52	19.12	80.62	0.66	18.66	73.81	0.65	19.12	69.99	0.01	18.85	62.27	0.00
2021/4	11:22:53	19.08	80.62	0.66	18.66	73.81	0.65	19.16	69.96	0.01	18.85	62.27	0.00
2021/4	11:22:54	19.08	80.62	0.65	18.66	73.81	0.65	19.12	69.96	0.00	18.85	62.30	0.00
2021/4	11:22:55	19.05	80.59	0.65	18.66	73.81	0.65	19.08	69.99	0.00	18.85	62.30	0.00
2021/4	11:22:56	19.08	80.65	0.66	18.71	73.81	0.65	19.16	70.02	0.00	18.90	62.27	0.00
2021/4	11:22:57	19.08	80.62	0.66	18.71	73.81	0.65	19.16	70.02	0.00	18.85	62.27	0.00
2021/4	11:22:58	19.05	80.62	0.65	18.66	73.81	0.65	19.12	70.02	0.00	18.90	62.30	0.00
2021/4	11:22:59	19.08	80.59	0.65	18.66	73.72	0.65	19.12	69.99	0.00	19.05	62.24	0.00
2021/4	11:23:00	19.08	80.62	0.65	18.66	73.72	0.65	19.12	69.99	0.00	18.85	62.27	0.00
2021/4	11:23:01	19.08	80.62	0.65	18.66	73.72	0.65	19.12	69.99	0.00	18.85	62.27	0.00
2021/4	11:23:02	19.12	80.62	0.65	18.66	73.72	0.65	19.08	69.96	0.00	18.80	62.24	0.00
2021/4	11:23:03	19.08	80.59	0.65	18.66	73.72	0.65	19.16	69.96	0.00	18.85	62.30	0.00
2021/4	11:23:04	19.08	80.59	0.65	18.66	73.75	0.65	19.16	69.96	0.00	18.90	62.30	0.00
2021/4	11:23:05	19.08	80.65	0.65	18.66	73.72	0.65	19.16	69.99	0.00	18.90	62.30	0.00
2021/4	11:23:06	19.05	80.59	0.65	18.66	73.72	0.65	19.16	69.99	0.00	18.85	62.27	0.00
2021/4	11:23:07	19.08	80.62	0.66	18.66	73.72	0.65	19.16	69.96	0.00	18.85	62.27	0.00
2021/4	11:23:08	19.08	80.59	0.65	18.71	73.72	0.65	19.08	69.99	0.00	18.90	62.30	0.00
2021/4	11:23:09	19.12	80.65	0.65	18.71	73.72	0.65	19.16	69.99	0.01	18.90	62.30	0.00
2021/4	11:23:10	19.08	80.62	0.65	18.66	73.72	0.65	19.16	70.05	0.00	18.90	62.30	0.00
2021/4	11:23:11	19.08	80.65	0.65	18.66	73.72	0.65	19.12	70.02	0.01	18.85	62.27	0.00
2021/4	11:23:12	19.08	80.65	0.65	18.66	73.72	0.65	19.12	70.02	0.00	18.90	62.30	0.00
2021/4	11:23:13	19.12	80.62	0.65	18.66	73.75	0.65	19.12	70.05	0.00	18.85	62.27	0.00
2021/4	11:23:14	19.12	80.62	0.65	18.71	73.72	0.65	19.12	70.05	0.00	18.90	62.30	0.00
2021/4	11:23:15	19.12	80.68	0.65	18.71	73.72	0.65	19.16	70.05	0.00	18.85	62.27	0.00
2021/4	11:23:16	19.08	80.65	0.65	18.66	73.72	0.65	19.16	69.99	0.00	18.85	62.27	0.00
2021/4	11:23:17	19.08	80.68	0.65	18.66	73.66	0.65	19.16	69.99	0.00	18.85	62.27	0.00
2021/4	11:23:18	19.08	80.65	0.65	18.66	73.66	0.65	19.16	69.99	0.00	18.85	62.27	0.00
2021/4	11:23:19	19.08	80.65	0.65	18.66	73.66	0.65	19.16	69.99	0.00	18.85	62.27	0.00
2021/4	11:23:20	19.08	80.65	0.65	18.66	73.66	0.65	19.16	69.99	0.00	18.85	62.27	0.00
2021/4	11:23:21	19.08	80.65	0.65	18.66	73.66	0.65	19.12	70.05	0.00	18.85	62.30	0.00
2021/4	11:23:22	19.16	80.65	0.65	18.66	73.66	0.65	19.12	70.05	0.01	18.90	62.30	0.00

Figure 4.5 Host computer data report interface[19]

4.1 Working condition settings

The main research direction of this chapter is to measure the temperature of the fuel cell, the single cell single voltage, and the battery power under different working conditions, so as to study and analyze the performance of the air-cooled fuel cell.

The temperature is measured by ten thermocouples evenly distributed on the wall of the fuel cell on the air side. The experimental steps are briefly described as follows: before each experiment, the air inlet valve is opened to purge the microchannels of the fuel cell. After the purge is completed, the corresponding parameters are set, and then the hydrogen valve is opened to allow the reaction to occur. After the parameters stabilize, data is recorded. After the experiment is completed, the hydrogen is turned off first, and the air valve is closed after the data drops to a reasonable range, and the experiment is ended.

The front view of the experimental stack is shown in Figure 4.6. The following discussion will focus on changing the fan voltage, hydrogen supply mode, and hydrogen pressure.

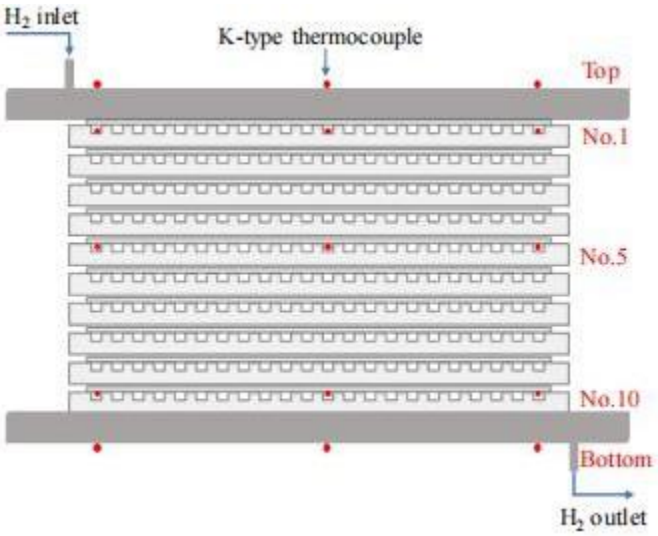

Figure 4.6 Front view of the experimental battery stack[19]

4.2 Influence of fan voltage

The experimental arrangement is shown in Table 4.1. The analysis focuses on three aspects: temperature, single voltage, and power. In each set of experiments, the fan voltage is fixed. Based on the actual experimental situation, the current is increased by 5A at intervals starting from 5A. The current is increased after the curve stabilizes for a period of time under the current current. The experiment is terminated when the curve becomes turbulent.

Table 4.1 Experimental conditions for changing fan voltage

Fan voltage	Group number	Current	Hydrogen pressure
5V	0-1	0-45A	0.6bar
6V	0-2	0-45A	0.6bar
8V	0-3	0-45A	0.6bar
10V	0-4	0-45A	0.6bar
12V	0-6	0-45A	0.6bar
13.8V	0-7	0-45A	0.6bar

Combining Figures 4.7, 4.8, 4.9, 4.10, 4.11, and 4.12 below, we can see that as the voltage increases, the temperature range within which the fan can operate normally and stably increases significantly. This can be understood as the fan speed increasing with the fan voltage, thereby increasing the amount of air intake, which in turn increases the amount of reactant oxygen, and thus the reaction intensity. As a result, the reaction heat generated increases, which manifests as a rise in the thermocouple temperature. However, at 13.8V, when the current reaches 60A, further increases in current intensity no longer significantly change the temperature, indicating that the

reaction intensity has reached saturation.

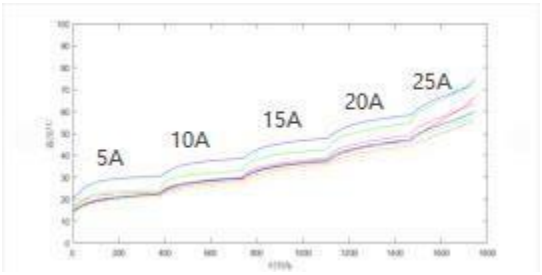

Figure 4.7 Temperature graph when the fan voltage is 5V

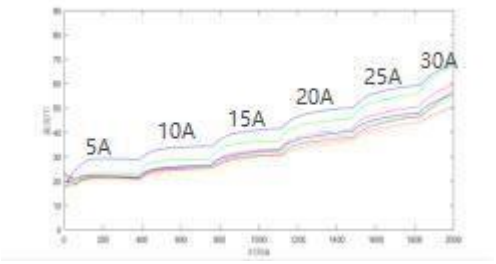

Figure 4.8 Temperature graph when the fan voltage is 6V

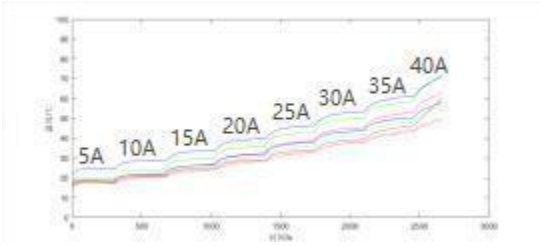

Figure 4.9 Temperature graph when the fan voltage is 8V

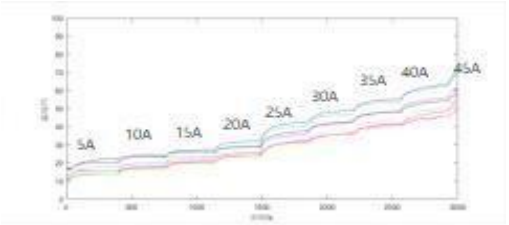

Figure 4.10 Temperature graph when the fan voltage is 10V

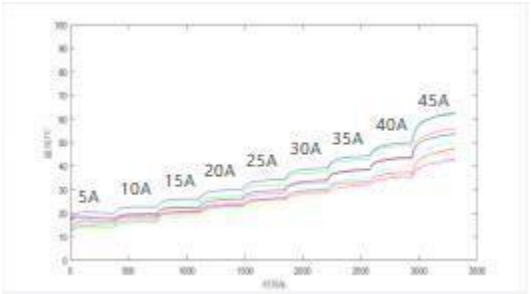

Figure 4.11 Temperature graph when the fan voltage is 12V

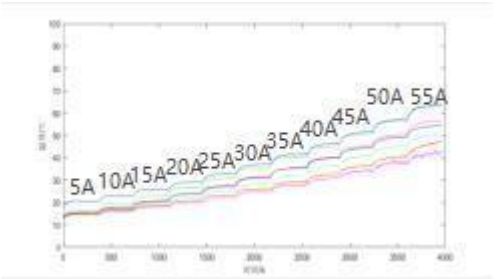

Figure 4.12 Temperature graph when the fan voltage is 13.8V

Combining Figures 4.13, 4.14, 4.15, 4.16, 4.17, and 4.18 below, we can see that at 13.8V, the voltage drop for a single chip and a single voltage is the largest. The trend in the magnitude of the voltage drop is that as the fan voltage increases, the voltage drop decreases, but not infinitely. Combined with the analysis of temperature and current variations in the previous section, we can see that as the fan voltage increases, the reaction intensifies, and the voltage drop range for a single chip and a single voltage also increases. Since the above figure shows the change trend of a single chip and a single voltage over time, and the single chip and a single voltage is the power supply voltage, the trend shown by the curve is consistent with actual theory.

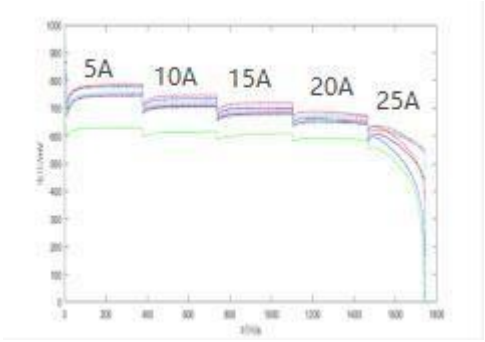

Figure 4.13 Voltage diagram when the fan voltage is 5V

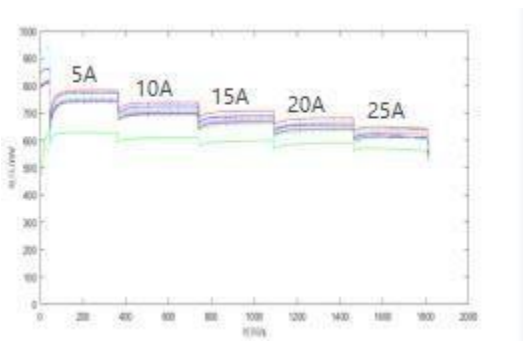

Figure 4.14 Voltage diagram when the fan voltage is 6V

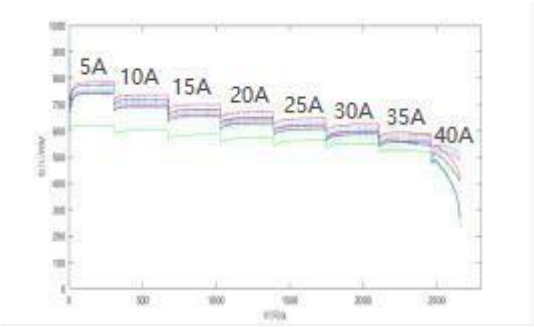

Figure 4.15 Voltage diagram when the fan voltage is 8V

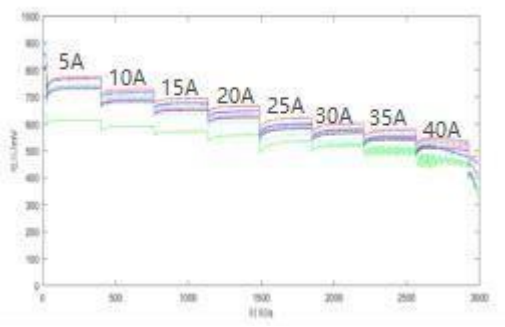

Figure 4.16 Voltage diagram when the fan voltage is 10V

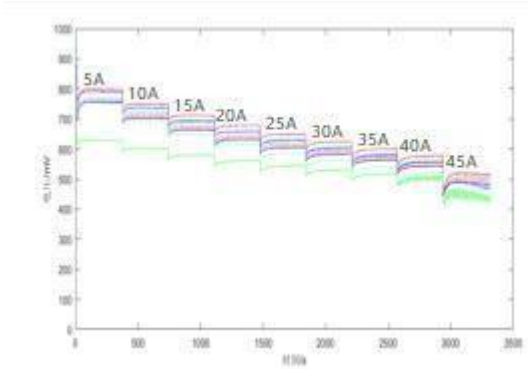

Figure 4.17 Voltage diagram when the fan voltage is 12V

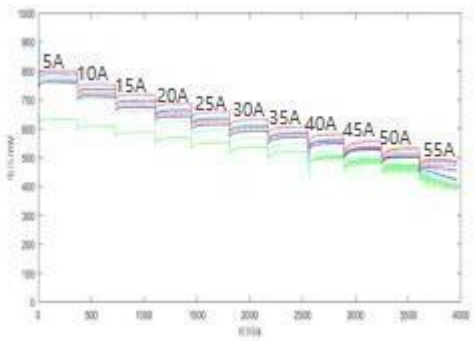

Figure 4.18 Voltage diagram when the fan voltage is 13.8V

Combining Figures 4.19, 4.20, 4.21, 4.22, 4.23, and 4.24, we can see that when the fan voltage is 5V, the maximum power is close to 150W, while when the fan voltage is 13.8V, the maximum power is close to 240W, and the power transition is more frequent, which can be understood as a more complete reaction of the battery stack.

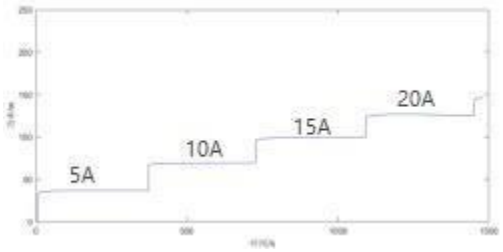

Figure 4.19 Electric power diagram when the fan voltage is 5V

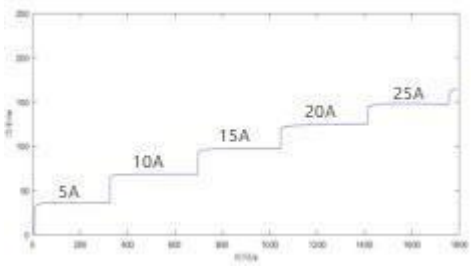

Figure 4.20 Electric power diagram when the fan voltage is 6V

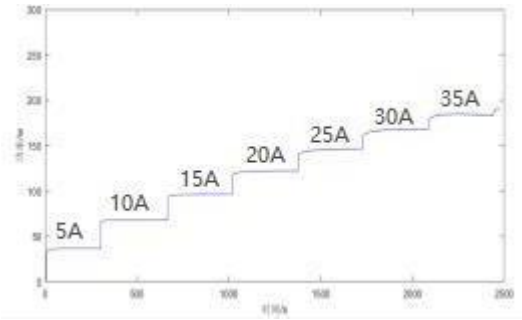

Figure 4.21 Electric power diagram when the fan voltage is 8V

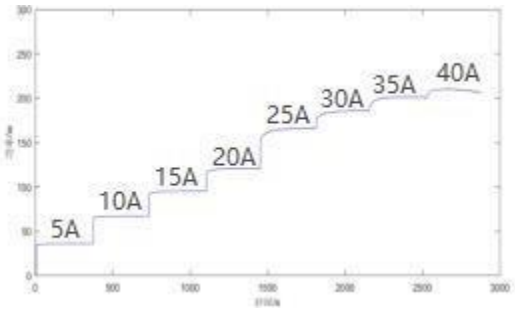

Figure 4.22 Electric power diagram when the fan voltage is 10V

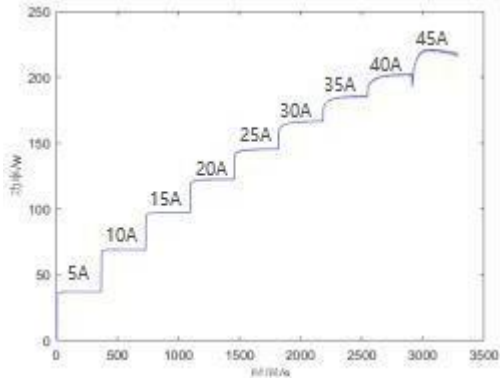

Figure 4.23Electric power diagram when the fan voltage is 12V

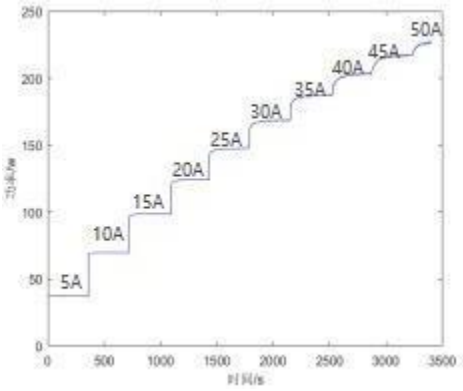

Figure 4.24 Electric power diagram when the fan voltage is 13.8V

4.3 Changing the hydrogen supply mode

The experimental arrangement is shown in Table 4.2. The analysis is conducted from three aspects: temperature, single voltage, and power. In each set of experiments, the fan voltage is fixed. Based on the actual experimental situation, the current is increased by 5A at intervals starting from 5A. The current is increased after the curve stabilizes for a period of time under the current current. The experiment is stopped when the curve becomes disordered. This section of the experiment requires three sets of control experiments with different hydrogen supply modes.

When the cathode-open PEMFC stack is operating, the hydrogen exhaust solenoid valve has three states: the first is always open, which is the flow-through mode or open hydrogen supply mode; the second is intermittent opening, which is the pulse exhaust mode or dynamic hydrogen supply mode; and the third is always closed, which is the closed-end hydrogen supply mode. When the stack is operating in the flow-through mode, the hydrogen inlet flow rate is a key factor affecting the stack's output performance and stability. Too little hydrogen flow will cause the stack to be short of gas, while too much hydrogen flow may remove a large amount of water from the membrane electrode, causing the membrane to dry out.

In the experiment of this section, no intermittent exhaust is the first circulation mode, intermittent exhaust is the second dynamic hydrogen supply mode, and closed-end hydrogen supply is the always closed mode. This section will analyze the effects of the three hydrogen supply modes on the fuel cell reaction through specific experiments.

Table 4.2 Experimental working conditions for changing hydrogen supply mode

Hydrogen supply mode	Group number	Current	Hydrogen pressure	Fan voltage
Continuous exhaust	0-3	0-45A	0.6bar	8V
Intermittent exhaust 20s/0.2s	1.2.1	15、25、35A	0.6bar	
Closed-end hydrogen supply	1.6.1	15A	0.6bar	

Combining Figures 4.25, 4.26, and 4.27, we used the control variable method, controlling the current to 15A, to analyze the impact of changes in the hydrogen supply mode on the fuel cell stack. The data for the uninterrupted exhaust should be taken from the third section from left to right, while the data for the intermittent exhaust of 20s/0.2s should be analyzed from the first section from left to right. From the figure for the uninterrupted exhaust, we can see that under stable conditions, the maximum thermocouple temperature is approximately 34°C, and the minimum is approximately 22°C; with intermittent exhaust of 20s/0.2s, the maximum thermocouple temperature is approximately 36°C, and the minimum is approximately 23°C; with closed-end hydrogen supply, the maximum thermocouple temperature is approximately 32°C, and the minimum is approximately 22°C. From the above experimental data, it can be seen that the impact of the hydrogen supply mode on the performance of the fuel cell stack is not very obvious. This does not mean that hydrogen supply has no effect on the performance of the fuel cell stack. Further refinement of the experimental conditions is needed.

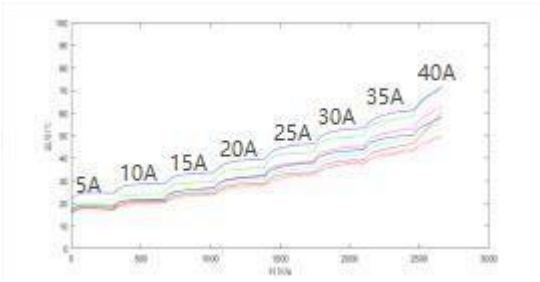

Figure 4.25 Gapless exhaust temperature diagram

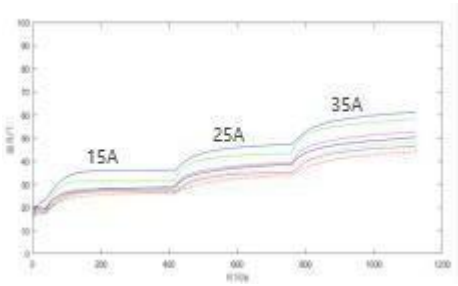

Figure 4.26 Temperature diagram of intermittent exhaust 20s/0.2s

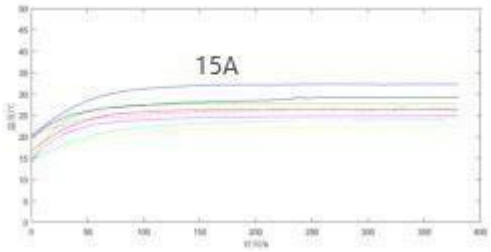

Figure 4.27 Closed-end hydrogen supply temperature diagram

From Figures 4.28, 4.29, and 4.30, we can see that the voltage variation of each cell is not very different. The highest voltage is over 700mV, and the lowest is around 610mV. This indicates that the exhaust method does not significantly affect the reaction intensity, that is, the intake volume is not affected.

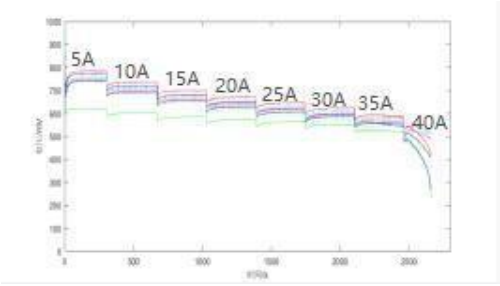

Figure 4.28 Gapless exhaust voltage diagram

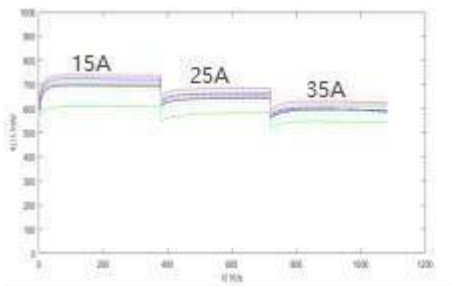

Figure 4.29 Voltage diagram for intermittent exhaust 20s/0.2s

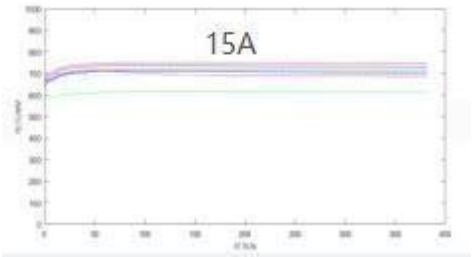

Figure 4.30 Closed-end hydrogen supply voltage diagram

Combining the content of 4.3.2 above and the data of the power change curves 4.31, 4.32, and 4.33, we can see that after the stack is running stably, the power of the stack is about 102W under the three working conditions, with little difference, which is consistent with the analysis in the previous section.

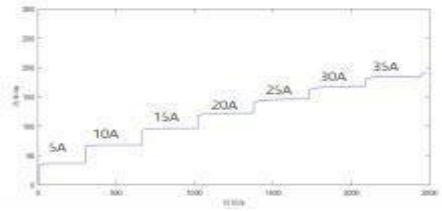

Figure 4.31 Gapless exhaust power diagram

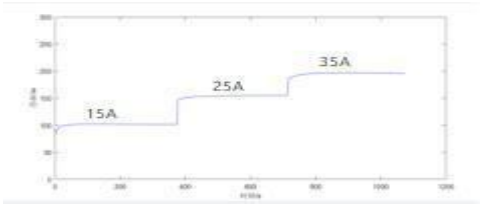

Figure 4.32 Intermittent exhaust 20s/0.2s electrical power diagram

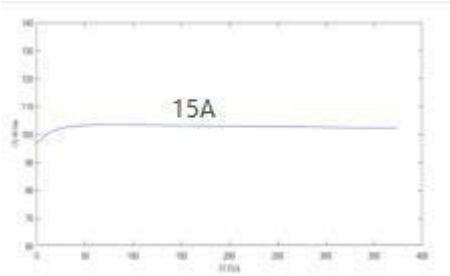

Figure 4.33 Closed-end hydrogen supply power diagram

4.4 Changing the hydrogen pressure

The experimental arrangement is shown in Table 4.3. The analysis is conducted from three aspects: temperature, single voltage, and power. In each set of experiments, the fan voltage is fixed. Based on the actual experimental situation, the current is increased by 5A at intervals starting from 5A. After the curve stabilizes for a period of time under the current current, the current is increased. The experiment is stopped when the curve becomes disordered.

The experimental conditions in this section are closed-end hydrogen supply, current intensity is 15A, fan voltage is 13.8V, and hydrogen pressure is changed to 0.4bar, 0.6bar, 0.8bar, and 1.0bar respectively, and experimental analysis is carried out.

When the fuel cell stack operates in closed-end hydrogen supply mode, the hydrogen supply pressure is an important factor affecting the fuel cell stack performance. The hydrogen supply pressure is closely related to the water content in the membrane. Too low a hydrogen supply pressure may also cause gas shortage in the fuel cell stack. Too high a hydrogen supply pressure may hinder the diffusion of water from the cathode side to the anode side, thereby affecting the fuel cell stack performance.

Table 4.3 Experimental conditions for changing hydrogen pressure in closed-end hydrogen supply mode

Hydrogen supply mode	Group number	Current	Hydrogen pressure	Fan voltage
Closed-end hydrogen supply	1.5.3	15A	0.4bar	Fan voltage 13.8V
	1.6.3	15A	0.6bar	
	1.7.3	15A	0.8bar	
	1.8.3	15A	1.0bar	

Combining Figures 4.34, 4.35, 4.36, and 4.37, we can see that the average temperature increase at each measurement location in the stack before and after thermal radiation under different hydrogen pressures is not much different. For cell No. 1, the temperature increase in closed-end hydrogen supply mode is higher than in pulse exhaust mode, and as the hydrogen pressure increases, the temperature increase of this cell also increases. This may be because, on the one hand, in closed-end hydrogen supply mode, the stack cannot remove some of the excess heat through hydrogen pulse exhaust, and at the same time, high hydrogen supply pressure hinders the diffusion of water from the cathode side to the anode, resulting in an increase in internal temperature. The temperature increase variation pattern of cells No. 5, No. 10, and the bottom end plate is similar to that of cell No. 1.

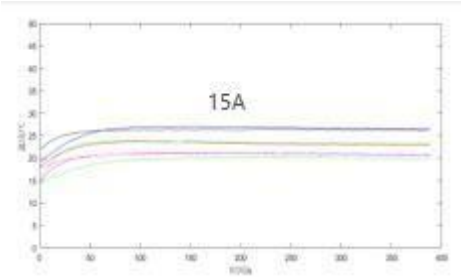

Figure 4.34 Hydrogen pressure 0.4 bar temperature diagram

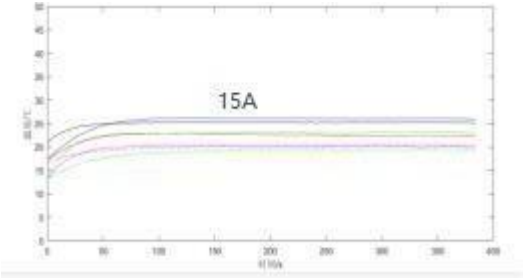

Figure 4.35 Hydrogen pressure 0.6 bar temperature diagram

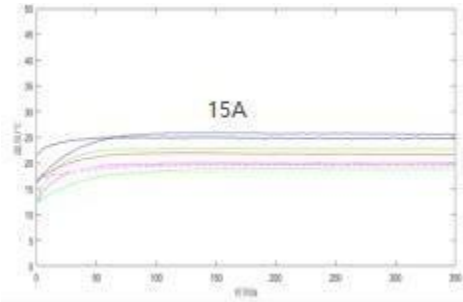

Figure 4.36 Hydrogen pressure 0.8 bar temperature diagram

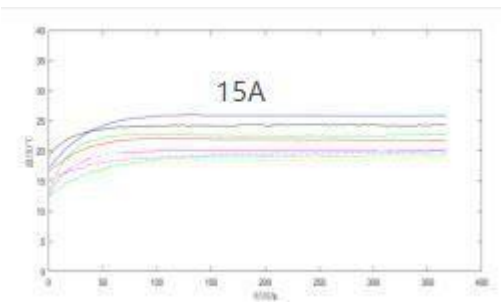

Figure 4.37 Hydrogen pressure 1.0 bar temperature diagram

According to Figures 4.38, 4.39, 4.40, and 4.41, under the experimental conditions of the

closed-end hydrogen supply mode with a current of 5A, as the hydrogen supply pressure increases, the decrease in the single voltage before and after the reaction decreases in a certain period of time. This phenomenon can be well explained by the Nernst effect. At the same time, when the hydrogen pressure increases to a standard atmospheric pressure, the voltage of the single cells 5, 7, and 9, which are farther away from the reaction source, does not decay, but increases. For example, the voltage of the single cell 9 increases by 19mV before and after the reaction. This phenomenon is mainly due to the fact that the radiant heat generated by the reaction weakens due to the increase in distance, and when the fuel cell reacts, the water generated inside the microchannel will be affected by the weakening of thermal radiation, and the flow of the gas-liquid two-phase flow will be improved. Here, cells 5, 7, and 9 are at the bottom of the cell stack. Due to the effect of gravity, the water generated by the anode reaction [28] accumulates at the bottom of the cell stack, thereby alleviating the trend of reducing the thickness of the water film on the inner wall of the cathode channel, thereby making the water heat management good.

Compared with the above-mentioned control group, the voltage drop of No.1, No.2, and No.3 cells, which are closer to the fuel reaction pair in the closed-end hydrogen supply mode, is not reduced significantly due to the change in hydrogen supply pressure in the closed-end hydrogen supply mode. For example, the voltage of No.2 cell decreased by 149mV, 132mV, and 86mV respectively when the hydrogen pressure was 0.04MPa, 0.06MPa, and 0.08MPa. Although it can be concluded from the Nernst effect that an increase in hydrogen pressure can reduce the drop in single voltage, according to the voltage attenuation value of 49mV in the control group, it can be seen that under the closed-end hydrogen supply mode, the increase in hydrogen supply pressure cannot effectively alleviate the effect of reaction heat on the voltage drop of the single cell. This is because the increase in hydrogen supply pressure will not only weaken the voltage attenuation of the single cell, but also increase the pressure of the water diffusion generated on the cathode side in the microchannel, hindering the flow of the water film, thereby exacerbating the membrane drying phenomenon caused by the strong heating effect due to the proximity to the reaction source.

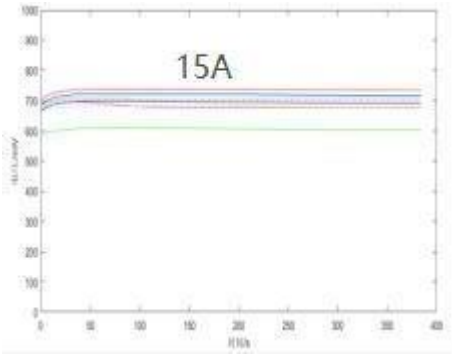

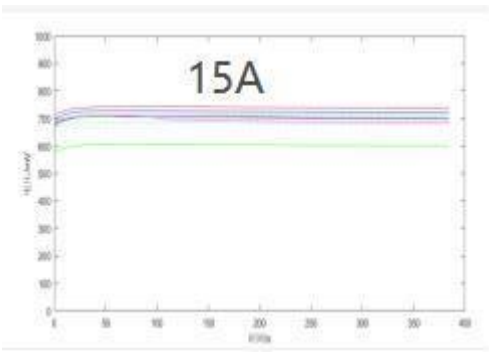

Figure 4.38 Voltage diagram at hydrogen pressure 0.4 bar

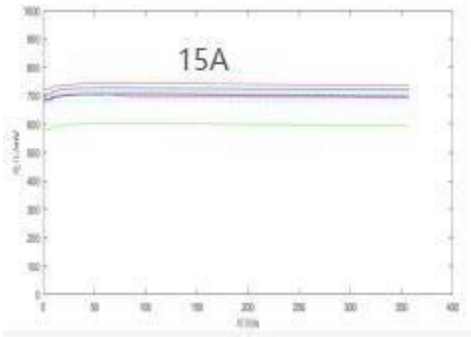

Figure 4.39 Voltage diagram at hydrogen pressure 0.6 bar

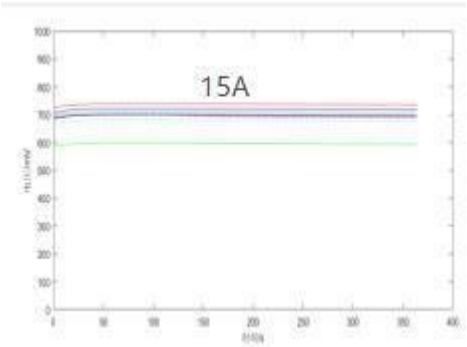

Figure 4.40 Voltage diagram at hydrogen pressure 0.8 bar

Figure 4.41 Voltage diagram at hydrogen pressure 1.0 bar

Figures 4.42, 4.43, 4.44, and 4.45 show the effect of anode gas pressure on stack performance degradation under thermal radiation in closed-end hydrogen supply mode. When the load current is set to 15A, Figure 4.42 shows that under closed-end hydrogen supply mode, at a hydrogen inlet pressure of 0.04 MPa, the stack output power decayed by 4.17 W before and after radiation, a significant increase compared to the 3.24 W of the reference group CG. However, as the inlet pressure increased, the stack power degradation before and after radiation significantly improved. For example, at a hydrogen pressure of 0.10 MPa, the power degradation value was only 0.51 W. According to the "Nernst effect" in fuel cells, increasing pressure can improve stack performance. Furthermore, increasing pressure enhances the diffusion capacity of hydrogen at the anode, thereby accelerating mass transfer, effectively reducing concentration polarization effects and increasing stack temperature.

In addition, under the closed-end hydrogen supply mode, under the condition of a hydrogen pressure of 0.06MPa, the power of the stack decreased by 3.12W before and after being heated by the reactor, which is lower than the voltage reduction value of 3.36W in the intermittent exhaust 20s/0.2s mode with the same hydrogen pressure. Therefore, it can be concluded that when the hydrogen supply pressure is kept the same, the closed-end hydrogen supply mode can effectively reduce the voltage drop caused by the heat of the reaction. Under normal temperature conditions, various experimental settings were carried out, and it was found that after the stack has been operating normally for a period of time, the electric power increased sharply at the beginning, then stabilized, and then dropped sharply until the stack stopped working. This is because in the closed-end hydrogen supply mode, the water that penetrated from the cathode to the anode cannot be discharged, resulting in water accumulation and flooding, which affects the

hydrogen supply flow at the hydrogen supply end, affects the reaction rate, and reduces the power of the stack.

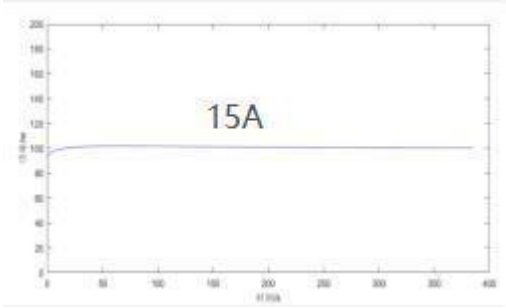

Figure 4.42 Electric power diagram of hydrogen pressure 0.4 bar

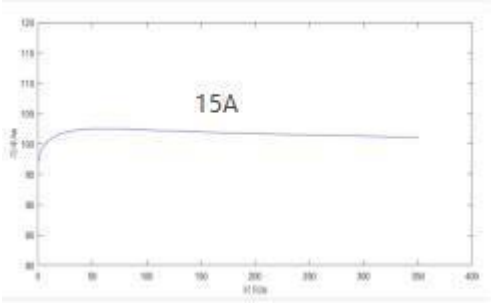

Figure 4.43 Electric power diagram of hydrogen pressure 0.6 bar

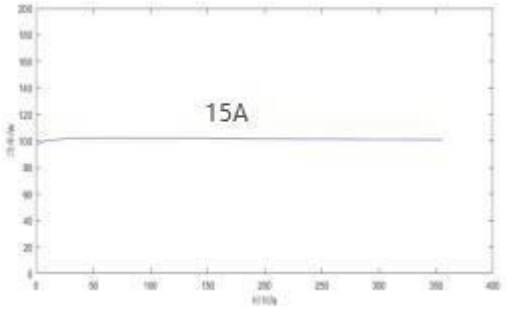

Figure 4.44 Electric power diagram of hydrogen pressure 0.8 bar

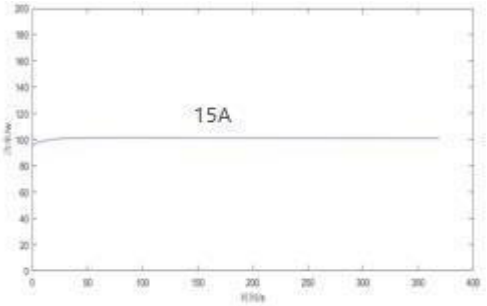

Figure 4.45 Electric power diagram of hydrogen pressure 1.0 bar

5. Conclusion and Outlook

5.1 Research Conclusions

This article outlines the classification and application of fuel cells and briefly explains the structure and working principle of proton exchange membrane fuel cells. It summarizes the influence of cathode open PEMFC stack structure and operating parameters on stack performance, and finds that there is less attention paid to the performance analysis of air-cooled stacks at home and abroad. Therefore, a fuel cell measurement and control platform designed and developed by Zhang Jiekai based on the performance parameters and test requirements of the experimental stack was used, and a series of performance research experiments on cathode open PEMFC stacks were carried out on the measurement and control platform. Key data such as stack output power, voltage, internal stack temperature, and single cell voltage were obtained, and the variation law of stack characteristic parameters was analyzed, and the stack operating parameter optimization strategy under high radiation intensity was obtained. However, there is no simulation of the wind field inside the fuel cell in the published literature at home and abroad. The simulation in this article is based on the analysis of many related models, and compared with the actual situation, certain optimization measures are obtained.

5.2 Wind field simulation

The conclusions drawn from the wind field simulation study are as follows:

(1) First, the establishment of the fluid domain is an approximate simulation based on the physical model, so more general conclusions can be drawn during the analysis;

(2) When setting the grid, we closely followed the actual research direction, focused on the grid division of the fuel cell microchannel, encrypted it locally, and finally highlighted the main conclusions;

(3) The wind field analysis shows that the wind fields on both sides of the microchannel are relatively strong. Since the wall is fixed and there is no slip, the wind speed on the wall side develops well. However, due to the influence of two large vortices, the wind field on the middle side of the microchannel develops relatively slowly, which is quite different from the actual working requirements.

5.2.1 Performance analysis

The conclusions drawn from the performance analysis study are as follows:

(1) Since the principle of air-cooled fuel cells is to rely on the reaction of hydrogen and oxygen, when the concentration of the reactants has not reached the reaction limit, increasing the fan voltage will increase the concentration of the reactant oxygen, thereby increasing the reaction amount, thereby increasing the reaction heat, increasing the single cell voltage drop, and

increasing the electrical power.

(2) The change of hydrogen supply mode actually changes the hydrogen flow rate. When the hydrogen supply mode is always in flow mode, the hydrogen inlet flow rate is an important factor affecting the output performance and stability of the fuel cell stack. Too little hydrogen flow rate will lead to gas shortage in the fuel cell stack, while too much hydrogen flow rate may carry away a large amount of water in the membrane electrode, causing the membrane to dry out. In the analysis conducted in this article, the impact of the change of hydrogen supply mode is not very obvious.

(3) When the fuel cell stack operates in closed-end hydrogen supply mode, the hydrogen supply pressure is an important factor affecting the fuel cell stack performance. The hydrogen supply pressure is closely related to the water content in the membrane. Too low a hydrogen supply pressure may also cause gas shortage in the fuel cell stack. Too high a hydrogen supply pressure may hinder the diffusion of water from the cathode side to the anode side, thereby affecting the fuel cell stack performance.

5.3 Research Prospects

The wind farm simulation and performance analysis research conducted in this paper is limited by the time limit for the graduation project and the lack of professional knowledge. There are still many areas for improvement and further exploration. The focus of subsequent work can be carried out in the following aspects:

(1) Wind field modeling can be performed by changing the distance between the fan and the microchannel or by changing the number of fans;

(2) The fan pressure drop difference can be used to convert the wind speed, which is closer to the actual working fan, and the influence of the actual impedance and the actual working environment must be considered. The wind field obtained in this way has a more general rule;

(3) The experimental device can be improved [29], and it is recommended to use high-definition cameras and thermal imagers to obtain more experimental results for analysis and research.

References

[1] Gu Liping. Fuel Cell Vehicles in Development and Improvement.[J]. Beijing Automotive, 2003, No.5

[2] National Energy Administration. Medium- and Long-Term Development Plan for the Hydrogen Energy Industry (2021-2035).March 23, 2022

[3] China Economic Information Network. Analysis of the Current Status of the Global and Chinese Hydrogen Fuel Cell Catalyst Industry: Developing Towards Low-Platinum and Non-Platinum Options.April 23, 2022

[4] Zhou Tong. Large Eddy Simulation of Ideal Mountain Wind Field Characteristics Under Atmospheric Boundary Layer Inflow.[D]. Civil Engineering, Beijing Jiaotong University, 2022-02-16

[5] Jin Bochong. Research on Simulation of Atmospheric Boundary Layer Wind Field Based on WRF and CFD Technology.[D]. South China University of Technology, 2020

[6] Li Yan, Yang Zhizhong, Sha Wenyu, Zhu Shouxian. Simulation of Sea Surface Pressure and Wind Fields in Typhoons.[J]. Marine Forecasts, 2003, Vol. 1, No. 6-13

[7] Zhang Futao. Study on Wave Simulation of a Typhoon Process Based on WAVE WATCH-III Model.[J]. China Harbor Engineering, 2019, No. 12: 46-50

[8] Cheng Xueling, Hu Fei, Zeng Qingcun.Detailed numerical simulation of wind field in complex terrain.[J]. Meteorological and Environmental Research, 2015, No. 1: 1-10

[9] Hiromori Miyagi, Koji Sasa. Experiment on the tornado generation environment using a multi-fan wind tunnel.[J]. PROCEEDINGS OF NATIONAL SYMPOSIUM ON WIND ENGINEERING, 2016, Vol. 24, No. 0: 133-138

[10] Simulation Study on Ventilation System of the Equipment Room for CCHP System.[J].Sustainable Energy,2015:49-59

[11] Gao Weitao, Lei Yijie, Zhang Xun, et al. Research Progress of Proton Exchange Membrane Fuel Cells[J]. Chemical Industry and Engineering Progress, 2021, 41(03): 1539-1555

[12] Xie Yichun, Zheng Liping, Lai Lianfeng, et al. Research on Temperature Stability Control of Proton Exchange Membrane Fuel Cell System.[J]. Times Automotive, 2021, (21): 109-111

[13] Yang Changxing, Zhao Runxian, Pan Ruixin, et al.Research Status of Hydrothermal Management of Air-Cooled Proton Exchange Membrane Fuel Cells.[J]. Power Technology, 2022, 46(04): 346-350

[14] Dai Liuliang.A Review of Simulation Analysis of Hydrothermal Management of Fuel Cell Engines.[D]. School of Energy and Power Engineering, Shandong University, 2021

[15] Zhang Shengsheng.Study on the catalytic agent and low temperature environment adaptability of proton exchange membrane fuel cell.[D]. Beijing

Jiaotong University, 2007, No. 03: 113

[16] Yang Zichu, Ding Gangyi, Sun Bowen, et al.Research on innovative design of portable hydrogen fuel cells based on field environment.[J]. Packaging Engineering, 2021, 42(10)

[17] Gao You.Design and Energy Consumption Economic Analysis of Hydrogen Fuel Cell Combined Heat and Power System.[D]. Hefei University of Technology, 2021

[18] Cai Niansheng. Application of proton exchange membrane in fuel cells[J]. Membrane Science and Technology, 1996, (04)

[19] Zhang Jikai. Experimental study on the performance of open cathode PEMFC under thermal radiation[D]. Hefei University of Technology, 2022

[20] He Qiang, Li Anling. Research on Key Technologies of High-Speed Precision Motorized Spindle Simulation[M]. 2018: 157-160

[21] Guo Xianchao.Internal Flow Simulation and Structural Improvement of Proton Exchange Membrane Fuel Cell Flow Channel.[D]. Dalian University of Technology, 2022

[22] Li Sunwei.OpenFOAM simulation of wind tunnel boundary layer wind field.[J]. Shanxi Architecture, 2008, 34(23): 70-71

[23] Zhang Qiunan. Numerical simulation of the impact of high-rise buildings on the diffusion of air pollutants[D]. Harbin University of Science and Technology, 2019

[24] Chen Yan, Zhang Jinyuan, Wang Nan, et al.Study on wind turbine wind field model and MATLAB numerical simulation of turbulent wind field.[J]. Acta Energiae Solaris Sinica, 2006, (09): 955-960

[25] Niu Jiangang, Chen Xu, Yan Liang.Numerical simulation of wind pressure distribution of conical tower structure of wind turbine in wind field.[J]. Journal of Inner Mongolia University of Science and Technology, 2017, 36(01): 84-92

[26] Super Energy Network.True Understanding of Cooling Fan Air Volume and Pressure.December 3, 2021

[27] Ruan Jingjie, Yi Chunming, Wu Xingyang.Design and performance research of air-cooled fuel cell.[J]. Metrology and Testing Technology, 2018, 45(09): 20-23

[28] Cai Niansheng.Water Balance in Solid Polymer Electrolyte Fuel Cells.[J]. Power Supply Technology, 1996, (03): 128-133

[29] Ma Xiaojun, Ke Rongshuo, Xu Shimeng, et al.Research on dynamic control of proton exchange membrane fuel cell system.[J]. Acta Armamentarii, 2012, 33(12): 1409-1415